NONLINEAR COMPENSATION IN OPTICAL COMMUNICATION SYSTEMS USING THE NONLINEAR FOURIER TRANSFORM

A Dissertation
Submitted to the Graduate Faculty
of the
North Dakota State University
of Agriculture and Applied Science

By

Thiago Diniz Sotero de Menezes

In Partial Fulfillment of the Requirements
for the Degree of
DOCTOR OF PHILOSOPHY

Major Department:
Electrical and Computer Engineering

July 2017

Fargo, North Dakota

NORTH DAKOTA STATE UNIVERSITY

Graduate School

Title

NONLINEAR COMPENSATION IN OPTICAL COMMUNICATION SYSTEMS USING THE NONLINEAR FOURIER TRANSFORM

By

Thiago Diniz Sotero de Menezes

The supervisory committee certifies that this dissertation complies with North Dakota State University's regulations and meets the accepted standards for the degree of

DOCTOR OF PHILOSOPHY

SUPERVISORY COMMITTEE:

Prof. Ivan T. Lima Jr
Chair

Prof. David Anthony Rogers

Prof. Sanjay Karmakar

Prof. Indranil Sengupta

Approved:

July 5, 2017
Date

Michael R. Kessler
Department Chair

ABSTRACT

Nonlinear effects in optical fibers impose a capacity limit for optical communication systems. In this dissertation, the nonlinear Fourier transform (NFT) is investigated as a method to mitigate and compensate for those effects. This study consists of two parts: first a computational complexity analysis for the use of the NFT for nonlinear compensation in the normal dispersion regime, and second, an analysis of the robustness of the performance of the discrete spectrum modulation in the anomalous dispersion regime using the NFT.

The first part investigates the computational complexity of the NFT based on the Zakharov-Shabat scattering problem as a nonlinear compensation technique for quadrature-phase-shift keyed (QPSK) signals with raised cosine frequency characteristic in optical fiber transmission systems with normal dispersion fibers. Results show that there are two primary sources of computational errors that arise from the use of the NFT: The computational error due to the finite eigenvalue resolution of the reflection spectra and the computational error due to the Born approximation used in the inverse NFT. In this scenario, computational costs become unacceptably large at data frame lengths and powers that are too small for this approach to be competitive with standard transmission methods.

The second part of this study investigates the robustness of a recently proposed nonlinear frequency-division multiplexing (NFDM) system comprised of two independent quadrature phase-shift keying (QPSK) channels modulated in the discrete spectrum associated with two distinct eigenvalues. We focus on determining the limits given by third-order dispersion, the Raman effect, amplified spontaneous emission (ASE) noise from erbium-doped fiber amplifiers (EDFAs), and lumped gain from EDFAs. Each of these impairments impact this system with discrete spectrum modulation and 1600 km of propagation distance in different ways: Third-order dispersion limits the maximum launch power to 13 dBm, the Raman effect limits the maximum launch power to 10.25 dBm, the ASE noise limits the maximum launch power to 9 dBm, while lumped gain limits the maximum launch power at 3.75 dBm.

Additional studies are needed to investigate the effectiveness of the NFT for discrete spectrum modulation formats with three or more eigenvalues.

ACKNOWLEDGEMENTS

I would like to thank my adviser Dr. Ivan Lima Jr. for all the support and guidance during this journey, for his patience and encouragement on the hard times. In special I want to thank him for his availability in all times of need. I want to thank the remaining members of the dissertation committee Dr. David Rogers, Dr. Sanjay Karmakar and Dr. Indranil Sengupta for the comments and feedback to make this a better dissertation and me a better professional. I would also like to thank Dr. Vladimir Grigoryan with Ciena Corporation and Dr. Curtis R. Menyuk, Dr. Valentin Besse and Chaoran Tu with University of Maryland Baltimore County for the conversations and insights on this research. I wish to thank my former supervisors Steve Gruver and Eric S. Christianson for their flexibility and assistance when I had to manage working and studying. Finally I would like to thank all my friends who have assisted me on the past 5 years helping me to complete this important step of my life, in particular for the spiritual mentoring, discipleship and fellowship of David Lindahl, Nathan Smolek and Daniel Castro.

DEDICATION

To my parents, Savio and Ione, to my sisters Amanda, Debora and Raquel, who always gave me unconditional love, unmeasurable support and endless encouragement in this journey, their sacrifices made my doctoral education possible.

TABLE OF CONTENTS

LIST OF TABLES

LIST OF FIGURES

LIST OF APPENDIX FIGURES

Figure Page

1. INTRODUCTION

1.1. Background

Optical fiber communication systems are a reliable and fast medium for long distance communication; most of the world's information travels over fiber optic networks as they serve as the backbone of the internet. The capacity of such systems have increased significantly, since its creation. However, in the past few years, the demand for higher capacity has increased even faster. As the capacity demand continue to increase rapidly, the communications systems should face a capacity shortage in the next decade [18].

In information theory, the Shannon limit defines what the capacity limit is for an specific channel in the presence of an all white Gaussian noise (AWGN). It is a good physical upper bound on the system capacity [39]. This limit is calculated based on the signal to noise ration (SNR) of a channel and it is true for low power optical communication systems; however, as the optical power increases the capacity reaches a maximum and starts to decay. This is caused by other optical fiber impairments that were not considered at the original Shannon limit calculation. Nonlinearity in optical fibers limits the achievable signal-to-noise ratio and, consequently, the transmission capacity of optical fiber communications systems [44]. To better describe the optical fiber capacities Essiambre et al. [17] proposed an analytical formula for nonlinear Shannon capacity limit:

$$C = \log_2\left(1 + \left[\frac{n_{sp} h\omega_0 \alpha L R_s}{P_0} + 4\frac{\gamma^2 P_a^2 L}{|R_s^2 \beta_2|}\right]^{-1}\right), \quad where \;\; P_a = \left[\sum_{n=N_{ch}/2(n\neq 0)}^{N_{ch}/2} \frac{\kappa}{2\pi}\frac{R_s}{|\Delta f_n|}\right]^{1/2} P_0 \quad (1.1)$$

In 1.1 C is the nonlinear capacity estimate, n_{sp} is the spontaneous emission factor relative to the amplifiers used in the system, $h\omega_0$ is the photon energy in J, α is the fiber loss coefficient in km^{-1}, L is the propagation distance, R_s is the symbol rate, p_0 average signal power, nonlinear coefficient γ, β_2 is the group-velocity dispersion and κ is a shaping factor (varies depending on the pulse and constellation used), N_{ch} is the number of channels in the system and Δf_n is the channel separation.

The principal source of nonlinearity in optical fibers is the Kerr nonlinearity, and it has been known since the 1980s that to lowest order in the nonlinearity strength and second-order dispersion, light propagation can be modeled by the nonlinear Schrödinger equation (NLS) [25], [33]. The NLS

is one of a very special class of nonlinear equations that can be solved using a nonlinear analogue of the Fourier transform [27], [2] that was first found by Zakharov and Shabat [48]. In general, this transformation will produce both a discrete (soliton) and continuous (reflection) spectrum. Due to the nonlinearity, the evolution of initial data in the time domain can be quite complex, but all this complexity disappears in the transform domain, and the evolution becomes linear and quite simple. It is this observation that is at the heart of efforts in the 1980s and 1990s to use solitons in communications systems, since the evolution of solitons is simple in systems that obey the NLS.

With the advent of coherent communications and advanced signal processing techniques in optical fiber communications systems, this basic idea has undergone a renaissance. Yousefi and Kschischang [45]–[47] have proposed to combine high-order soliton solutions with advanced signal processing techniques to achieve high spectral efficiency. Experimental studies have demonstrated that it is possible to implement this idea for at least low-order soliton solutions [15].

Turitsyn and colleagues [28, 29] have proposed to encode information in the continuous spectrum, as opposed to the discrete spectrum.. This proposal has several attractive features. First, the continuous spectrum reduces to the usual Fourier transform at low intensities, so that it is possible to carry over standard modulation formats in a straightforward way. Second, a continuous spectrum can be generated in both the normal and the anomalous dispersion regimes, while a discrete spectrum (solitons) can only be generated in the anomalous dispersion regime.

1.2. Objectives

The goal of this research is to investigate the capabilities of the Nonlinear Fourier Transform (NFT) as a possible candidate to mitigate the nonlinear impairments on optical fiber communication systems; to overcome the capacity limits imposed by Kerr nonlinearity. Furthermore, it is to build a platform to verify how efficient, robust to the physical impairments, and computational costly some of the most promising NFT methods are. Therefore, a continuous spectrum modulation method was studied in a normal dispersion regime and compared to traditional linear methods on its complexity and efficiency. In addition, a discrete spectrum modulation format was tested for robustness in the anomalous regime.

1.3. Organization

The dissertation is organized as follows: Chapter **??** presents the study on the effectiveness of the continuous spectrum modulation using the NFT, with a description of the limitations of the use

of this modulation technique. Chapter 3 presents the results of the analysis of the effectiveness of the discrete spectrum modulation with respect to the following optical fiber impairments: inter-symbol interference, gain and loss, Raman effect and third-order dispersion. Chapter 4 is a discussion on the overall results and implications for future research topics resulting from this research.

2. NORMAL DISPERSION REGIME: CONTINUOUS SPECTRUM[1]

2.1. Background

While the idea of using the continuous spectrum is attractive, work to date has pointed to several issues that must be addressed if this idea is going to have practical value. First, the computational complexity of carrying out the analogue of the Fourier transform and its inverse is high. The NFT and its inverse (INFT) are given by the solution to the Zakharov-Shabat scattering problem (ZSSP). In the forward direction, the most widely used computational methods have a computational complexity that is proportional to N^2, where N is the number of points in the waveform that is being processed [1, 7]. In the backward direction (INFT), the most commonly used methods have a computational complexity that is either proportional to N^2 in differential layer peeling methods [40] or $N^2 \log N$ in the integral layer peeling method [35]. The complexity of these methods scale too rapidly with N to be acceptable in practice, and there is recent work indicating that it is possible to find algorithms in both directions that scale proportional to $N \log^m N$, where m is a small positive integer [5]. However, more work must be done to determine the practicality and robustness of these approaches.

Work to date has pointed to the possible existence of two additional, more fundamental problems. The NFT and the INFT rely fundamentally on the assumption that the signal is zero at the edges of the time domain that is being considered and that the second-order dispersion is constant along the transmission. For these reason, the data must be carved into data frames that reside inside larger signal frames or total time frames that are sufficiently large to accommodate any spread in the data that is due to second-order dispersion. In this respect, these systems resemble orthogonal frequency domain multiplexed (OFDM) systems [30]. In studies to date of the NFT and INFT in both the normal [42, 32] and anomalous [28] dispersion regimes, the data frame only

[1]The material in this chapter was co-authored by Thiago D. S. DeMenezes and Dr. Ivan Lima Jr. Thiago D. S. DeMenezes had the responsibility for generating some of the simulation results, figures and tables. Dr. Ivan Lima Jr. lead the submission of this chapter as a journal paper and both participated on the review process.

occupies a small fraction of the total time frame. In the normal dispersion regime, the fraction occupied was a little over 1% [42]; in the anomalous dispersion regime, the fraction occupied was a little over 10% [28]. There are reasons to believe that there may be a fundamental limit to the size of the data frames. In the normal dispersion regime, the waveform encoding the symbols act as barriers in the forward ZSSP. As the reflection coefficient approaches 1 with the increase in the frame duration, the waveform containing the symbols in the center of the data frame become increasingly difficult to resolve. In the anomalous dispersion regime, for a fixed power, standard estimates indicate that the number of solitons should grow with the data length [2].

Just as there may be limits on the size of the data frames, there may be limits on the signal power within those frames. In the anomalous dispersion regime, increased power is expected to lead to soliton generation [2]. In the normal dispersion regime, it becomes increasingly difficult to resolve bits in the center of the data frame.

This chapter explains in detail the scaling of the back end processing time as both the size of the data frame and signal power within the data frame increase for the same quaternary-phase-shift-keyed (QPSK) format that Le et al. [28], studied, although the focus here is on the normal dispersion regime. One of the findings is that the use of the NFT and the INFT in the signal processing results in a computational error in the calculation that grows exponentially with the channel power and the data frame duration. For realistic fiber parameters, the onset of this exponential growth occurs at a combination of signal powers and data frame lengths that are too low for this scheme to be competitive as an alternative to standard quasilinear transmission. When the channel power is set to 3 dBm in a QPSK modulation format at 56 Gbaud with 512 symbols per data frame, the number of points required to discretize the reflection spectra exceeds 2^{103}. It is important to highlight that this exponential increase in the back end processing time is not due to the computational complexity of the algorithms. Rather, it is a fundamental limit due to both the increase in the error due to the Born approximation and the rapid increase in the resolution of the reflection spectra that is required to decode the waveform when the channel power and the number of symbols per data frame are large.

Because these issues are fundamental, they will arise with any data format, and the limits that they impose should be determined when investigating a data format's performance.

The remainder of this chapter is organized as follows: Sec. 2.2 reviews the ZSSP and describes the computational algorithms that were used to solve the NFT and INFT and the motivation for these choices. In Sec. 2.3 the numerical results relating the computational cost of the NFT and the INFT as a function of the launch power and the frame duration. Sec. 2.4 describes the underlining reasons for the exponential increase of the computational cost of the NFT and the INFT with both the launch power and the frame duration. The limits on the data frame length and signal power are surprisingly low compared to quasilinear systems. Section 2.5 contains the conclusion.

2.2. Numerical Methods

The time and the space dependence of the slowly varying envelope of the optical signal propagating in optical fibers is modeled by the nonlinear Schrödinger (NLS) equation [3],

$$i\frac{\partial A(t)}{\partial z} + i\frac{\alpha(z)}{2} - \frac{\beta_2}{2}\frac{\partial^2 A(t)}{\partial t^2} + \gamma\left|A(t)\right|^2 A(t) = 0, \tag{2.1}$$

where $A(t)$ is the slowly varying envelope of the optical signal that also depends implicitly on z, the space coordinate along the direction of propagation, γ is the nonlinear parameter, β_2 is the second-order dispersion, and $\alpha(z)$ is the attenuation coefficient or gain. The most efficient techniques to solve the NLS equation in optical fiber communications systems is the split-step Fourier method. In the particular case in which the losses can be either neglected or mitigated through the use of distributed amplification ($\alpha \cong 0$), the normalized slowly varying envelope of the optical signal $q(t)$ satisfy the ZSSP, which is defined in terms of the equations [48]

$$\begin{aligned}\frac{du(t,\zeta)}{dt} &= i\zeta u(t,\zeta) + q(t)v(t,\zeta),\\ \frac{dv(t,\zeta)}{dt} &= -i\zeta v(t,\zeta) + q^*(t)u(t,\zeta),\end{aligned} \tag{2.2}$$

where $u(t,\zeta)$ and $v(t,\zeta)$ are the eigenfunctions of the ZSSP associated to the eigenvalue ζ. To apply the ZSSP in (2.2) to optical fibers with the slowly varying envelope of the optical signal $A(t)$, the expression 2.3 is used.

$$q(t) = \sqrt{\frac{\gamma}{|\beta_2|}}A(t). \tag{2.3}$$

The term $(\gamma/|\beta_2|)^{1/2}$ in (2.3) is the normalization coefficient of the ZSSP, so that (2.2) can be applied to lossless optical fibers with arbitrary nonlinear parameter γ and second-order dispersion β_2. The eigenfunctions $u(t,\zeta)$ and $v(t,\zeta)$ also depend implicitly on z, but the eigenvalue ζ, is a conserved quantity that, consequently, does not change with the propagation.

The QPSK frame of symbols is located near the center of the computation time window $[0, T_w]$ with boundary conditions $A(0) = A(T_w) = 0$. The left and the right reflection spectra at the receiver are given by

$$r_L(\zeta) = \left.\frac{v(0,\zeta)}{u(0,\zeta)}\right|_{v(T_w,\zeta)=0}, \quad r_R(\zeta) = \left.\frac{u(0,\zeta)}{v(0,\zeta)}\right|_{u(0,\zeta)=0}. \tag{2.4}$$

The advantage of using the reflection spectra to represent the waveform, compared to the Fourier spectrum, is that the magnitude of the reflection spectra at each eigenvalue ζ does not change with z if the medium does not have losses. Moreover, the phase of the reflection spectra evolves linearly, so that the reflection spectra calculated at the receiver can be forward or backward to any point along propagated z using a single propagation step that compensates for the combined effects of nonlinearity and dispersion along the transmission. The reflection spectra at the transmitter ($z = 0$) can be computed from the calculated reflection spectra at the receiver ($z = L$) using the equations

$$\begin{aligned} r_L(\zeta,0) &= r_L(\zeta,L)\mathrm{e}^{+i2\zeta^2\beta_2 L}, \\ r_R(\zeta,0) &= r_R(\zeta,L)\mathrm{e}^{-i2\zeta^2\beta_2 L}. \end{aligned} \tag{2.5}$$

It is the resolution in ζ that is required to accurately determine the original data that in turns determines the value of T_w. In practical cases, the value of T_w is much larger than that of a single data frame.

2.2.1. Nonlinear Fourier Transform

This study makes use of the piece-wise constant approximation (PCA) to calculate the NFT [7] or, equivalently, to solve the direct scattering problem. Most studies so far have made use of only the left reflection spectrum. However, there is no computational cost required to calculate the right reflection spectrum together with the left reflection spectrum using the PCA method. Moreover, there is also little additional computational cost in using both the left reflection spectrum,

to construct the first half of the time-domain waveform of the optical signal in our computation of the INFT, and the right reflection spectrum, to construct the second half of the time-domain waveform, in our computation of the same INFT. The most efficient methods to compute the INFT are based on iterative procedures, whose computational error accumulates as the number of iterations increases. The computational error in the symbols near the right end of the frame dominate the overall computational error of INFT procedures that use only the left reflection spectrum. Therefore, the error in our computation of the INFT is significantly reduced when the waveform is reconstructed from both ends of the data frame in time domain.

To calculate both the left and the right reflection spectra using the PCA, the procedure described in [40] was used. For every eigenvalue ζ, it calculates the evolution of the eigenfunctions during each time-step,

$$\begin{bmatrix} u\left(t_{n+1}\zeta\right) \\ v\left(t_{n+1}\zeta\right) \end{bmatrix} = \mathbf{T}_{n+1}(\zeta) \begin{bmatrix} u\left(t_{n}\zeta\right) \\ v\left(t_{n}\zeta\right) \end{bmatrix}, \tag{2.6}$$

where

$$\mathbf{T}_n(\zeta) = \begin{bmatrix} \cosh(k\Delta_t) & q(t_n)\sinh(k\Delta_t) \\ +i\zeta\sinh(k\Delta_t) & \\ q^*(t_n)\sinh(k\Delta_t) & \cosh(k\Delta_t) \\ & -i\zeta\sinh(k\Delta_t) \end{bmatrix}, \tag{2.7}$$

and $k^2 = |q|^2 - \zeta^2$. Then the transmission matrix is calculated

$$\mathbf{T}(\zeta) = \prod_{n=0}^{N-1} \mathbf{T}_n(\zeta) \tag{2.8}$$

for a given eigenvalue ζ, the left and the right reflection spectra in (2.2) can be calculated,

$$r_L(\zeta) = \frac{-T_{2,1}(\zeta)}{T_{2,2}(\zeta)}, \quad r_R(\zeta) = \frac{T_{1,2}(\zeta)}{T_{2,2}(\zeta)}. \tag{2.9}$$

The eigenvalue spectral range is defined from $-\pi/(2\Delta_t)$ to $\pi/(2\Delta_t)$. If the eigenvalue range is discretized with N_{pt} points, the eigenvalue resolution is given by $\Delta_\zeta = \pi/(N_{\text{pt}}\Delta_t)$. The eigenvalues of the ZSSP computed are evenly spaced because practical INFT methods make use of the Fourier transform and/or the inverse Fourier transform of the reflection spectra. The computa-

tional complexity of the PCA is proportional to $N_{\text{samp}} \times N_{\text{pt}}$, where the constant of proportionality is the number of operations used to evaluate the 2×2 complex matrix in (2.5) and to carry out a 2×2 complex matrix multiplication.

2.2.2. Inverse Nonlinear Fourier Transform

The first computational method to solve the INFT consisted of integral equations developed by Gel'fand, Levitan, and Marchenko [13]. However, due to the high computational complexity required to directly solve the Gel'fand-Levitan-Marchenko (GLM) integral equations (N^3), more efficient iterative methods have been developed [40, 35, 41, 19, 12, 14, 6].

The differential layer peeling (DLP) method is one of the most efficient INFT methods [12]. The DLP method exploits causality to iteratively solve the GLM integral equations with computational complexity proportional to $N_{\text{samp}} \times N_{\text{pt}}$, where N_{samp} is the number of samples used to discretize the waveform in time domain, and N_{pt} is the total number of points used to discretize the left reflection spectrum [40, 19, 12]. The DLP method that is applied to fiber grating design requires that the reflection coefficient from within a discrete space step be small enough so that the reflection coefficient of that layer can be lumped at the end of the discrete space step [19]. Otherwise, the computational error in the result produced by the DLP algorithm, which increases exponentially along the direction of the profile extraction, would be unacceptably high. For that reason, strong gratings, in which the reflection coefficient is close to 1 over a large spectral band, require a large number of steps along the grating for the DLP to produce accurate results. In the optical fiber communications problem considered, a QPSK modulation format with -3 dBm of channel power and 56 dB per data frame requires time steps that are significantly smaller than the symbol period.

Rosenthal and Horowitz [35] developed an inverse scattering algorithm–denoted integral layer peeling (ILP) method–that consists of solving the GLM integral equations for each layer using an iterative procedure that includes the recursive calculation of the local reflection spectrum, starting with the left reflection spectrum in (2.9). Because the errors in the ILP accumulate with the number of iterations, as it is the case in the other iterative methods for calculating the INFT, the choise was to implement and use the symmetric ILP (SILP) method. In the SILP method, the left portion of the waveform is computed from the left edge of the waveform up to the center of the time window, using the left reflection spectrum. Then, the right portion of the waveform is

computed from the right edge of the waveform until the center of the time window, using the right reflection spectrum.

The SILP method uses the Born approximation to define the local reflection spectra at the time $t_{m+1} = t_m + \Delta_t$,

$$\begin{aligned} r_{L,m+1}(\zeta) &= \frac{r_{L,m}(\zeta) - \bar{r}_{L,m}(\zeta)}{1 - r_{L,m}\bar{r}^*_{L,m}(\zeta)} \mathrm{e}^{-i2\zeta\Delta_t}, \\ r_{R,m+1}(\zeta) &= \frac{r_{R,m}(\zeta) - \bar{r}_{R,m}(\zeta)}{1 - r_{R,m}\bar{r}^*_{R,m}(\zeta)} \mathrm{e}^{-i2\zeta\Delta_t}, \end{aligned} \tag{2.10}$$

where

$$\begin{aligned} \bar{r}_{L,m}(\zeta) &= \int_{-\infty}^{2\Delta_t} h_{L,m}(\tau)\mathrm{e}^{i\zeta\tau} d\tau, \\ \bar{r}_{R,m}(\zeta) &= \int_{(\pi/\Delta_\zeta)-2\Delta_t}^{\infty} h_{R,m}(\tau)\mathrm{e}^{-i\zeta\tau} d\tau, \end{aligned} \tag{2.11}$$

and

$$\begin{aligned} h_{L,m}(\zeta) &= \int_{-\infty}^{\infty} r_{L,m}(\tau)\mathrm{e}^{-i\zeta\tau} d\tau, \\ h_{R,m}(\zeta) &= \frac{1}{2\pi}\int_{-\infty}^{\infty} r_{R,m}(\tau)\mathrm{e}^{i\zeta\tau} d\tau, \end{aligned} \tag{2.12}$$

are the Fourier transform of the left-local reflection spectrum and the inverse Fourier transform of the right-local reflection spectrum, respectively. The local reflection spectra at $m = 0$ is the reflection spectra calculated with the PCA algorithm in (2.9). The recovered waveform at the discrete time $t_m = m\Delta_t$ is given by:

$$A(t_m) = \sqrt{\frac{\beta_2}{\gamma}} \times \begin{cases} -h_{L,m}(t_{m+1}), \ m \le N_{\mathrm{samp}}/2 \\ \\ h_{R,m}(t_{N_{\mathrm{samp}}-m+1}), \ m > N_{\mathrm{samp}}/2 \end{cases} . \tag{2.13}$$

Since only N_{samp} values of the time-domain waveform are generated by the SILP metthod, whose reflection spectra has a much larger number of discrete values, N_{pt}, it is necessary to shift the time

in the reflection spectra prior to the execution of the iterative procedure in (2.10)–(2.13):

$$r_{L,0}(\zeta) = r_L(\zeta)\mathrm{e}^{-i\zeta\Delta_t(N_{\mathrm{pt}}-N_{\mathrm{samp}})/2},$$
$$r_{R,0}(\zeta) = r_R(\zeta)\mathrm{e}^{-i\zeta\Delta_t(N_{\mathrm{pt}}-N_{\mathrm{samp}})/2}. \tag{2.14}$$

The SILP method is capable of extracting the profile of gratings whose reflection coefficient is very close to 1 across a wide spectral band. The computational error of the SILP method does not accumulate as fast as with the DLP method, enabling the SILP method to reconstruct gratings with reflectivity as large as $1 - 10^{-10}$ [35]. Even though the computational complexity of the SILP is $N_{\mathrm{samp}} \times N_{\mathrm{pt}} \cdot \log N_{\mathrm{pt}}$, as needed to solve (2.10)–(2.13), this method converges significantly faster than the DLP method when applied to strong gratings, which correspond to optical signals with channel power close to -3 dBm.

Belai, et al., developed an alternative method to solve the GLM integral equations based on the iterative inversion of Toeplitz matrices obtained from the GLM integral equations that was denoted Toeplitz inner-bordering (TIB) [6] which has numerical complexity equal to N_{pt}^2 when the iterative matrix inversion procedure is optimized. However, in [6], the authors pointed out that the TIB method is only adequate to extract the profile with gratings with a maximum reflectivity up to 99.9% because of the large increase of the computational error with the iterative matrix inversion procedure. When these results are extended to optical fiber communications systems operating in the normal dispersion regime, the maximum magnitude of the reflection spectra that the TIB can operate corresponds to the linear/quasi-linear regime of operation.

Due to the higher robustness of the SILP method in the nonlinear regime, in which the magnitude of the reflection spectra is very close to 1 over a wide range of the eigenvalue ζ, the choice was the SILP method to calculate the INFT in this study.

2.2.3. Modulation Format

The simulation uses each data frame with a sequence of symbols using the QPSK modulation format with raised cosine frequency characteristics as in [34]. Simulation also includes the raised cosine frequency characteristic using the matched receiver filter, in which the transmitted signal has the root raised cosine frequency characteristic, and the receiver filter has a transfer function

$H(f)$ with the root raised cosine frequency characteristic given by

$$H(f)=\begin{cases} 1, \ \dfrac{1-\epsilon}{2T_s} \\ \cos\left[\dfrac{\pi T_s}{2\epsilon}\left(|f|-\dfrac{1-\epsilon}{2T_s}\right)\right], \ \dfrac{1-\epsilon}{2T_s}<|f|\leq\dfrac{1+\epsilon}{2T_s} \\ 0, \ |f|>\dfrac{1+\epsilon}{2T_s} \end{cases}, \tag{2.15}$$

where T_s is the symbol period per data frame and ϵ is the roll-off factor.

The algorithms chosen to carry out the NFT-INFT computation (PCA and the SILP) are applied to the waveform before the receiver filter. These could in principle be implemented experimentally by applying a digital filter whose transfer function is close to the inverse of the receiver filter in (2.15) after the signal is demultiplexed and optically filtered at the receiver. Then, after the left and the right reflection spectra are digitally propagated backward to the transmitter and the waveform is extracted from the reflection spectra using the SILP method, the signal is passed through a filter whose transfer function is shown in (2.15).

2.2.4. Channel Power and Effective Symbol Rate

In addition to the requirement that the transmission systems do not have losses for the eigenvalues to remain constant during the fiber transmission, the nonlinear parameter γ, along with the second-order dispersion β_2, must remain constant. Therefore, each data frame with a fixed number of symbols has to be separated by a guard time that is large enough to ensure that the dispersed frames do not produce inter-data frame cross-talk along the transmission due to the nonlinearity and, more importantly, they do not produce inter-data frame interference at the receiver.

Therefore, the requirement of the guard time leads to a reduction in the channel power, given the average power per data frame, and a reduction in the effective symbol rate, given the symbol rate in the data frame. The guard time t_g required to accommodate for the dispersion along the fiber transmission is given by

$$t_g = t_{g,R} \times 2\pi|\beta_2| f_{s,\mathrm{df}} \cdot L, \tag{2.16}$$

Table 2.1. The ratio (in dB) of the channel power and the average launch power per data frame (P_{ch}/P_{df}), the effective symbol rate (f_s), and the spectral efficiency (SE) for a QPSK modulation format at 56 GBd per data frame as a function of the number of symbols per data frame for 1000 km of propagation distance.

Symbols/Frame	P_{ch}/P_{df}(dB)	f_s(GHz)	SE (bits/s/Hz)
32	-6.7	11.9	0.43
64	-4.5	19.7	0.70
128	-2.8	29.1	1.04
256	-1.7	38.3	1.37
512	-0.9	45.5	1.62

where $f_{s,\mathrm{df}}$ is the symbol rate in the data frame, $t_{g,R}$ is the relative guard time, and L is the length of the fiber transmission system. In the results shown here, simulaiton used $t_{g,R} = 1.2$, which provides a 20% margin for the guard time, as in [28]. Given the guard time in (2.16), the channel power P_{ch} is given by

$$P_{\mathrm{ch}} = \frac{N_{\mathrm{sym}}}{N_{\mathrm{sym}} + t_g \cdot f_{s,\mathrm{df}}} P_{\mathrm{df}}, \tag{2.17}$$

where P_{df} is the average power per data frame and N_{sym} is the number of symbols per data frame. The effective symbol rate f_s is given by

$$f_s = \frac{N_{\mathrm{sym}}}{N_{\mathrm{sym}} + t_g \cdot f_{s,\mathrm{df}}} f_{s,\mathrm{df}}. \tag{2.18}$$

Table I shows the difference in dB between the average launch power and the channel power in dB, the ratio between the symbol rate per data frame and the effective symbol rate, and the spectral efficiency for 56 GBd QPSK systems with 32, 64, 128, 256, and 512 symbols per data for 1000 km of propagation distance.

Therefore, it is desirable to have the number of symbols per data frame as large as possible in order to minimize the performance degradation due to the guard time. Conversely, as previously discussed, increasing the size of the data frame or the power leads to a rigid increase in the spectral resolution that is required to accurately implement any computational INFT algorithms. It is the tradeoff between these requirements that limits the performance.

2.2.5. System Model and Performance Metric

The Q-factor calculated from the error-vector magnitude (EVM) [37, 36] was used as the performance metric for the computational errors from the nonlinear compensation using the NFT . Each simulation consists of the following steps:

1. Generation of the QPSK waveform from a randomly-chosen data frame and propagation through all the spans of a lossless and noise-free optical fiber transmission system modeled by (2.1) using an adaptive split-step method.
2. Application of the PCA method to the received waveform.
3. Propagation of the reflection spectra in the backward direction to the transmitter using a single step, as shown in (2.5).
4. Reconstruction of the waveform at the transmitter using the SILP.
5. Addition of a time-shift in the frequency domain on half the time step to cancel the time shift between the NFT and the INFT;
6. The reconstructed waveform is filtered using the transfer function in (2.15).
7. Calculation of the EVM in the data frame.
8. Repeat the steps 1-6 30 times, and calculate the Q-factor from the average EVM. In a QPSK system, the Q-factor is given by

$$Q = \left(\frac{1}{N} \sum_{n=1}^{N} \mathrm{EVM}_n \right)^{-1}. \tag{2.19}$$

The Q-factor is calculated using 30 randomly-chosen data frames to reduce the variance in the calculation.

2.3. Results

Computer simulations were used to assess the effectiveness of signal processing techniques based on the ZSSP applied to optical fiber communications systems in the normal dispersion regime. The optical fiber that is considered has second-order dispersion $\beta_2 = 5$ ps^2/km and nonlinear parameter $\gamma = 1.27$ (W·km)$^{-1}$. These parameters are close to those of commercially available

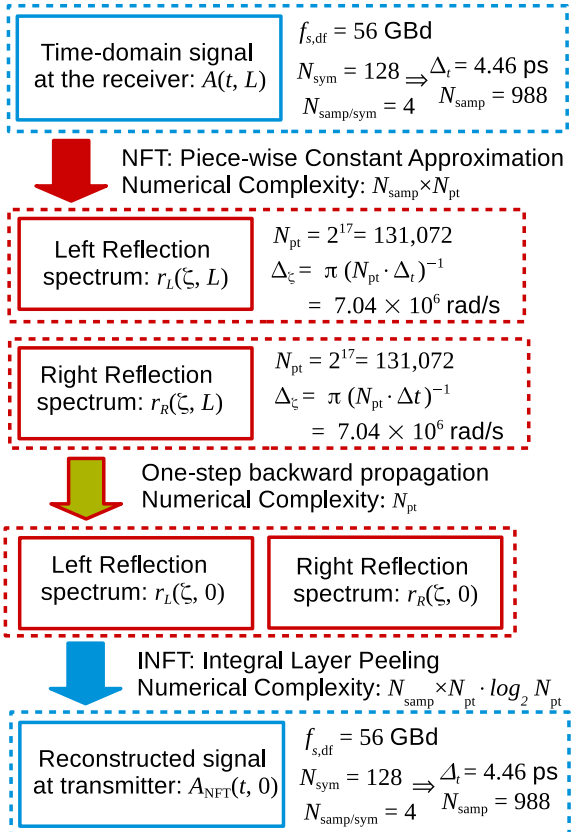

Figure 2.1. Schematic diagram of the nonlinear mitigation technique based on the NFT. It uses here the PCA to compute the NFT and the SILP to compute the INFT. The numbers here are applicable to a QPSK waveform with 128 symbols at 56 GBd per data frame and -2.9 dBm of channel power (0 dBm of average power per data frame) with 4 samples per symbol and relative guard time $t_{g,R} = 1.2$, resulting in a total of $(128 + 119) \times 4 = 988$ samples. The reflection spectra are discretized with 2^{17} points.

single-mode fiber and to those used in [42]. The total propagation distance consider here is equal to $1,000$ km. The QPSK modulation format was used with the raised cosine spectral characteristic described in Sec. 2.2.3 with a roll-off factor $\epsilon = 1/7$. The PCA method is used to solve the NFT and the SILP method that was presented in Sec. 2.2.2 to solve the INFT. When executing the PCA and the SILP methods, the computational cost of those methods is minimized by only calculating the NFT and the INFT for the smallest number of samples in the time domain that are sufficient to accommodate the frame duration and the guard time. Figure 2.1 shows the schematic representation of the steps 1 through 4 shown in Sec. 2.2.5 applied to a QPSK system with 128 symbols at 56 GBd per data frame with a channel power equal to -2.9 dBm. The number of points

used to discretize the reflection spectra, $N_{\text{pt}} = 2^{17}$, is the smallest number of points–in powers of two–that produces a $Q > 15$ dB due to discretization errors in the PCA-ILP algorithms.

2.3.1. Reflection Spectra

This sub-section investigates the dependence of the reflection spectra resolution on the channel power. Unlike the equivalent representation of the waveform in the Fourier domain, the reflection spectra in (2.4) and (2.9), which accounts for the combined effects of nonlinearity and dispersion along the fiber transmission, are also dependent on the channel power.

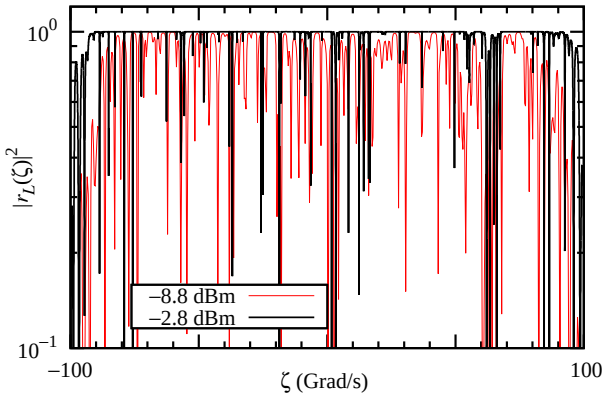

Figure 2.2. Squared magnitude of the left reflection spectrum as a function of the eigenvalue ζ for channel power equal to -8.9 dBm (with 2^{10} points) with 2 samples per symbol and -2.9 dBm (with 2^{17} points) with 4 samples per symbol with 128 QPSK symbols per symbol at 56 GBd per data frame with $1,000$ km of lossless propagation distance and relative guard time $t_{g,R} = 1.2$, which corresponds to and effective symbol rate of 29 GBd.

Figure 2.2 shows the squared magnitude of the left reflection spectrum of a QPSK waveform at 56 GBd per data frame with 128 symbols, $1,000$ km of lossless propagation distance, and relative guard time $t_{g,R} = 1.2$, which corresponds to an effective symbol rate of 29 GBd. The left reflection spectrum is shown at -8.9 dBm of channel power (-6 dBm of average power per data frame) with 2 samples per symbol and -2.9 dBm of channel power (0 dBm of average power per data frame) with 4 samples per symbol. The number of samples per symbol used in each case was the minimum number of samples that enabled $Q > 15$ dB due to numerical errors in the NFT-INFT algorithms. The system with -8.9 dBm of channel power has a left reflection spectrum whose magnitudes are clustered toward 1, but vary broadly between 0 and 1. By contrast, in the system with -2.9 dBm of channel power, the magnitude of the non-zero left reflection spectrum is close to 1 at almost all

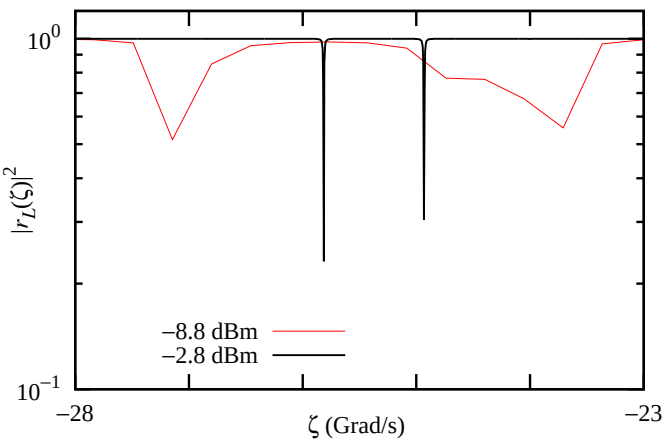

Figure 2.3. The same results shown in Fig. 2.2 for the eigenvalue ζ from -28 to -23 Grad/s.

values of ζ. However, the left reflection spectrum is punctuated by a set of sharp spikes that must be resolved in order to accurately calculate the INFT.

The largest value of the left reflection spectrum magnitude with -2.9 dBm of channel power is equal to $1 - 1.9 \times 10^{-9}$, while the largest value of the left reflection spectrum magnitude with -8.9 dBm of channel power is equal to 0.9993. The maximum possible value that the reflection spectra magnitude in (2.9) in a system with positive second-order dispersion can take is equal to 1, as in the case of fiber Bragg gratings, and it should approach 1 as the channel power or the number of symbols per data frame increase. Therefore, optical fiber communications systems with normal dispersion fibers and distributed gain that compensates for the fiber loss have reflection spectra that are very close to 1 at channel powers as low as -2.9 dBm with as little as 128 symbols per data frame. If the channel power in this system is increased to as little as -1.2 dBm of channel power (1.7 dB of average power per data frame), the magnitude of the left reflection spectrum in at least one of the eigenvalues ζ becomes so close to 1 that it exceeds the accuracy of the floating point numerical representation with double precision, which leads to numerical errors in any INFT algorithm that makes use of the reflection spectra, regardless of the spectral resolution that is used.

In Figure 2.3, which was generated using a sub-set of the data showed in Figure 2.2, results show that the QPSK waveform with -2.9 dBm of channel power (0 dBm of average power per data frame) requires a much higher eigenvalue resolution of the reflection spectra than the same waveform with -8.9 dBm of channel power (-6 dBm of average power per data frame). With a power of

-8.9 dBm of channel power and 2^{10} points in the reflection spectra, it has $Q = 20.0$ dB. With a power of -2.9 dBm of channel power and 2^{17} points in the reflection spectra, it has $Q = 16.6$ dB.

To quantify the rapid increase of the required eigenvalue resolution of the reflection spectra with the channel power, it is also calculated the maximum value of the magnitude of the derivative of the left reflection spectrum with respect to the eigenvalue ζ for the results shown in Figure 2.2. For -8.9 dBm of channel power, the maximum value of the derivative of the left reflection spectrum with respect to the eigenvalue ζ was equal to 5.80×10^9 (rad/s), while for -2.9 dBm of channel power the corresponding number was equal to 3.73×10^7 (rad/s). Therefore, a factor of four increase in the channel power produces an increase of two orders of magnitude in the derivative of the left reflection spectrum with respect to the eigenvalue ζ. These results indicate that there is a trade-off between the channel power and the eigenvalue resolution of the NFT, which is one of the main factors that determines the computational cost of the algorithm.

2.3.2. NFT and Channel Power

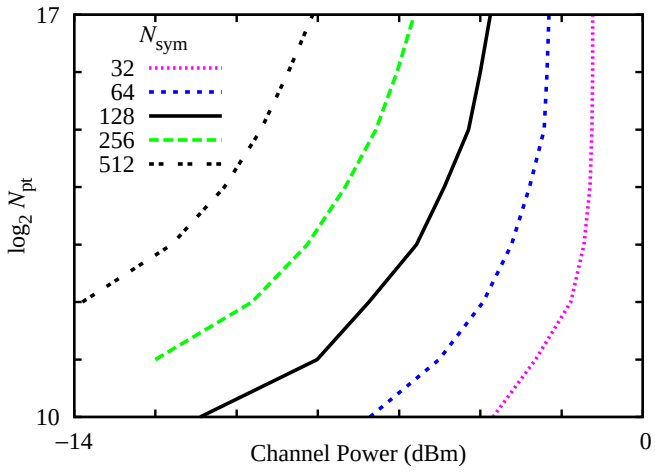

Figure 2.4. The logarithm with base 2 of the number of points used to discretize the reflection spectra as a function the channel power and $Q > 15$ dB due to the numerical error of the NFT-INFT algorithms. The symbol rate per data frame is equal to 56 GBd and the relative guard time $t_{g,R} = 1.2$. The results are parametrized by the number of symbols per data frame. The Q-factor is calculated from the EVM using 30 randomly-chosen data frames.

In the previous sub-section, it is indicated that the eigenvalue resolution required to apply the NFT to a frame with 128 QPSK symbols at -2.9 dBm of channel power was orders-of-magnitude higher than the eigenvalue resolution required to apply the NFT to the same QPSK frame with

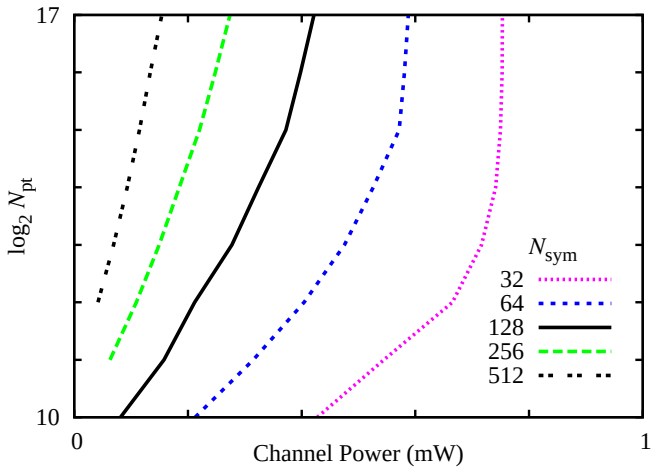

Figure 2.5. Same results shown in Figure 2.4 presented with the average power given in mW.

−8.9 dBm of channel power. To investigate the dependence of the computational error of the NFT-INFT algorithms that were used on the channel power, the number of points used to discretize the reflection spectra, and the number of symbols per data frame, this studied carried out a channel power sweep for eight different number of points used to discretize the reflection spectra: 2^{10}, 2^{11}, 2^{12}, 2^{13}, 2^{14}, 2^{15}, 2^{16}, and 2^{17} points, and five different number of symbols per data frame: 32, 64, 128, 256, and 512 symbols. For every channel power, it was determined the number of points required in powers of two to discretize the reflection spectra that results in $Q > 15$ dB from the average EVM due to discretization errors in 30 randomly-chosen data frames with the NFT-INFT algorithms. Since the number of samples per symbol in these cases was equal to 4 and the range of eigenvalues ζ is fixed, the increase in the number of points used to represent the reflection spectra increases only the resolution of the reflection spectra.

The results of this study are shown in Fig. 2.4 with the relative guard time $t_{g,R} = 1.2$. At 56 GBd per data frame, the effective symbol rates of: 11.9 GBd for 32 symbols per data frame, 19.7 GBd for 64 symbols per data frame, 29.1 GBd for 128 symbols per data frame, 38.3 GBd for 256 symbols per data frame, and 45.5 GBd for 512 symbols per data frame. Figure 2.5 shows the same results in Figure 2.4 presented with the channel power in linear scale (in mW). It was found that the number of points required to discretize the reflection spectra increases exponentially or faster with the channel power. For the QPSK system with 512 symbols to operate at $Q > 15$ dB

at 3 dBm, it can be extrapolated from the results in Figure 2.5 that the reflection spectra has to be discretized with at least 2^{103} points, which is not computationally feasible.

The faster than exponential growth at high-channel power levels is also due to spectral broadening along the transmission that leads to an increase in the guard time beyond the allocated amount with 20% guard time margin used ($t_{g,R} = 1.2$). Therefore, even if the numerical complexity of the NFT-INFT algorithms could be made as low as that of the Fourier transform ($N \log N$), the computational cost of using the existing NFT-INFT algorithms to encode/decode data would not be practical even when the system is operating in the quasi-linear regime.

2.3.3. NFT and Time Discretization

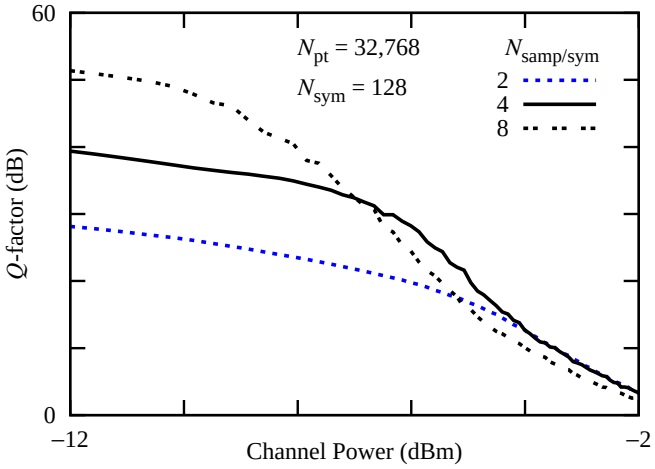

Figure 2.6. Q-factor of the received waveform as a function of the channel power for a QPSK waveform with 128 symbols and 56 GBd per data frame with relative guard time $t_{g,R} = 1.2$. The reflection spectra are discretized with 2^{15} points with 2, 4, and 8 samples per symbol. The Q-factor is calculated from the EVM using 30 randomly-chosen data frames.

Figure 2.6 shows the Q-factor due to numerical error in the NFT-INFT algorithms for a QPSK waveform with 56 GBd of symbol rate per data frame and relative guard time $t_{g,R} = 1.2$ as a function of the channel power for 2, 4, and 8 samples per symbol with the reflection spectra discretized with 2^{15} points. At channel power below -10 dBm, the use of larger number of samples per symbol produces more accurate results, as shown in Fig. 2.6. In the linear regime of operation, the residual numerical error reduces by 12 dB for every doubling of the number of samples per

symbol. This residual error is the result of the Born approximation, whose accuracy increases with the decrease of Δ_t.

As the average power per data frame increases for a fixed number of samples peer symbol, the computational error in the calculation of the INFT also increases. This increase in the computational error with the channel power is due to the Born (zero-order) approximation [35], which in the SILP method, numerically lumps the reflection from each step at the end of the step. The computational error due to the Born approximation increases with the average power, and accumulates with each iteration of the SILP method. It was found that, the Q-factor decreased slowly with the increase of channel power until reaching a channel power threshold beyond which the Q-factor decreases much faster with the average power due to the limited resolution of the reflection spectra. Therefore, the computational error in the results shown in Fig. 2.6, before the Q-factor decreased rapidly with the channel power, is the result of the Born approximation, which produces a computational error that increase as the average power increases. Hence, the Born approximation is one of the effects that limits the use of the NFT-INFT algorithms for nonlinear mitigation even in the quasi-linear regime.

Using the DLP algorithm in [19], the magnitude of the lumped local reflectance in (2.6) at the end of a time step Δt is given by:

$$|\rho| = \tanh\left[\sqrt{\frac{\gamma}{|\beta_2|}}|A(t)|\Delta_t\right]. \tag{2.20}$$

The Born approximation requires that $\rho \ll 1$. Since the optical fiber under consideration has the normalization coefficient of the ZSSP in (2.3) is given by

$$\sqrt{\frac{\gamma}{|\beta_2|}} = 5.04 \times 10^{11}\ \mathrm{W}^{-1/2} \cdot s^{-1}, \tag{2.21}$$

it was found that the average power per time step has to stay below -3 dBm at 224 Gsamp/s per data frame for $|\rho| < 5\%$ at the center of a symbol. This rate corresponds, for example, to 56 Gbd per data frame with 4 samples per symbol. For 128 QPSK symbols per data frame with relative guard time $t_{g,R} = 1.2$, this limit corresponds to -5.9 dBm of channel power. As the magnitude of the local reflection increases, the Born approximation becomes less accurate, leading to an increase

in the computational error of the calculation of the waveform in each layer with duration Δ_t. This error accumulates during the layer peeling procedure.

The magnitude of the lumped local reflection per layer close to the center of the symbols calculated for the results shown in Fig. 2.6 at -12 dBm of channel power are 5%, 2.5%, and 1.2% for 2, 4, and 8 points per symbol, respectively. These values of the lumped local reflection per layer (time step Δ_t) are much smaller than 1, as required by the Born approximation. However, at 0 dB of channel power, the corresponding magnitude of the local reflection is 19.7%, 9.9%, and 4.9% for 2, 4, and 8 samples per symbol, respectively. Therefore, the computational error that results from the use of the Born approximation increases as the average power per data frame increases, which requires an increase in the number of samples per symbol used in the INFT algorithm. If the channel power is increased to 3 dBm, it would be necessary to have at least 16 samples per symbol to achieve $|\rho| < 5\%$. Since the Fourier bandwidth of the waveform increases very little due to the nonlinear effects in the quasi-linear regimes that this research investigated, this increase in the number of samples per symbol that is needed to satisfy the Born approximation in the SILP method, or other INFT methods that make use of the Born approximation, can in principle be accomplished by interpolating the sampled values from the waveform.

The zero-order numerical approximation that is actually used in the numerical discretization of the SILP is given in terms of the kernel functions and the Fourier transform of the reflection spectra. Even though the computational error due to the Born approximation in the SILP is also due to a zero-order approximation as in the DLP method, the computational error in the former accumulates slower than in the latter during the iterative layer peeling procedure because of the higher numerical robustness of the SILP method.

2.3.4. NFT and Number of Symbols per Data Frame

In Figure 2.5, the performance of the computational NFT in a QPSK modulation format at 56 GBd per data frame with 128 symbols per data frame and a minimum allowed value of $Q = 15$ dB due to numerical error. The maximum power was limited to -4 dBm using $N_{\text{pt}} = 2^{17}$ to discretize the reflection spectra. For a minimum allowed $Q = 15$ dB and 2^{17} points to discretize the reflection spectra for 256 and 512 symbols per data frame it is observed that the channel power decrease to -6 dBm and -8 dBm, respectively. Figure 2.7 shows that the computational cost of

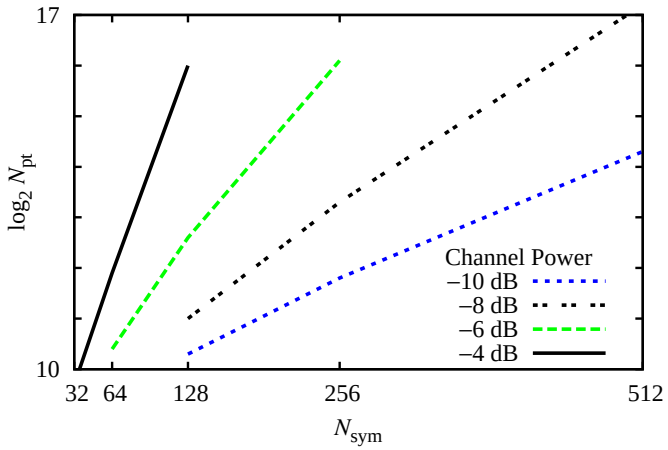

Figure 2.7. The logarithm with base 2 of the number of points used to discretize the reflection spectra as a function the number of symbols per data frame (in linear scale) for $Q > 15$ dB due to the numerical error of the NFT-INFT algorithms. The symbol rate per data frame is equal to 56 GBd and the relative guard time $t_{g,R} = 1.2$. The results are parametrized by the channel power. The Q-factor is calculated from the EVM using 30 random data frames.

the NFT-INFT algorithms increases exponentially with the number of symbols for a fixed channel power.

2.4. Reflection Spectra Resolution

The numerical results shown in the previous section indicate that the eigenvalue resolution of the reflection spectra and, consequently, the computational cost of the NFT-INFT algorithms increases rapidly as the system moves from the linear to the quasi-linear regime of operation. The nonlinear effects in the optical fiber transmission system without in-line dispersion compensation, which requires the use of a fixed frame followed by a guard time, increase as a result of the increase in the channel power, in the number of symbols per data frame, or both. Since the practical viability of using computational NFT-INFT algorithms for nonlinear compensation in optical fiber communications systems depends significantly on the computational cost of the method, it is important to understand the reason for the interdependence between the computational cost of the NFT-INFT algorithms and both the channel power and the number of symbols per data frame. In what follows, an intuitive explanation is given for the rapid growth in computational cost with both the channel power and the data frame length.

2.4.1. Reflection Spectra and Computation Time Window

Since the NFT based on the ZSSP described in Sec. 2.2 has a fixed value of the nonlinear parameter γ and the second-order dispersion β_2, there is always a finite propagation distance at which the non-zero region of the waveform centered at $T_w/2$ would disperse beyond the limits of the computation time window: $[0, T_w]$. Since T_w is in practical cases far larger than the signal frame, this distance will typically be larger than the propagation distance of $1,000$ km. However, this distance always exists in the normal dispersion regime ($\beta_2 > 0$), since this regime does not support solitons. Once the waveform exceeds the upper or the lower limit of the simulation time window due to the chromatic dispersion, the signal appears at the opposite end of the simulation window in our computational algorithm due to the intrinsic periodicity that arises from the use of a finite eigenvalue resolution Δ_ζ of the reflection spectra that was used to numerically represent the waveform. In case studied, the eigenvalue resolution is given by $\Delta_\zeta = \pi/(N_{\mathrm{pt}}\Delta_t)$ and $T_w = N_{\mathrm{pt}}\Delta_t$. The eigenvalue resolution Δ_ζ will be the same for any other INFT algorithm that makes use of the fast Fourier transform. If the signal is still propagating nonlinearly when the periodic wrapping occurs, then the computational window is not large enough to resolve the nonlinear evolution. In this case, the INFT algorithm must produce a large error at any distance since its accuracy is the same at all distances.

Figure 2.8 shows the relative root-mean-square (RMS) width of the Fourier spectrum of a QPSK waveform with 128 symbols at 56 GBd per data frame with relative guard time $t_{g,R} = 1.2$ as a function of the propagation distance. The initial RMS width of the spectrum waveform at the origin is equal to 32.5 GHz. The RMS width of the Fourier spectrum increases until the dispersed waveform spreads out so much that the nonlinear effects become negligible or the dispersed waveform exceeds the simulation window. The total duration of the dispersed data frame T_{df} in the quasi-linear regime as a function of the propagation distance L is given by:

$$T_{\mathrm{df}} = N_{\mathrm{sym}} \cdot \frac{1}{f_{s,\mathrm{df}}} + 2\pi|\beta_2| f_{s,\mathrm{df}} \cdot L. \tag{2.22}$$

For the simulation with 2^{11} (for -8.9 dBm of channel power), 2^{13} (for -5.9 dBm of channel power), and 2^{17} (for -2.9 dBm of channel power) to discretize both the reflection spectra and the time window of simulation, the size of the periodic window is: 3.90×10^3 km, 15.5×10^3 km, and

331×10^3 km, respectively. These are the number of points used to discretize the reflection spectra that are the minimum to enable $Q > 15$ dB due to numerical error in the NFT-INFT algorithms. Note that the number of points required to discretize the time window in most of the systems operating in the quasi-linear regime that were investigated here is much larger than the number of points required to discretize the reflection spectra, since the actual propagation distance that is considered, $L = 1,000$ km, is short compared to the propagation length in which the nonlinear effect is significant, as illustrated in Figure 2.8. In the practical cases in which the number of samples recovered in time domain, N_{samp}, is smaller than the number of points used to discretize the reflection spectra, N_{pt}, the time shift in (2.14) has to be used.

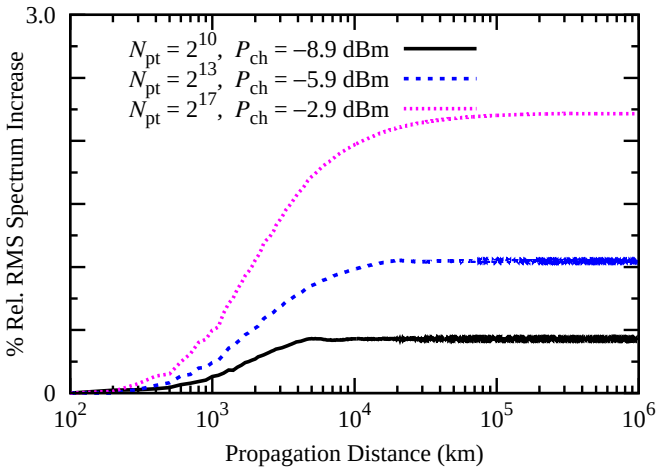

Figure 2.8. The evolution along the fiber of the relative RMS width of the Fourier spectrum of the waveform that consists of 128 QPSK symbols with 56 GBd of symbol rate per data frame with relative guard time $t_{g,R} = 1.2$ for -8.9 dBm, -5.9 dBm, and -2.9 dBm of channel power with of channel power with 2^{11}, 2^{13}, and 2^{17} points to discretize both the reflection spectra and the time window of simulation, respectively. The results are calculated from the average of 30 random data frames.

2.4.2. Equivalence to Fiber Bragg Gratings

The left reflection spectra associated to the eigenvalues ζ in the ZSSP in (2.2) that models lossless transmission in optical fiber systems with normal dispersion is equivalent to the reflectance spectrum of a fiber Bragg grating, which can also be described by (2.2) [7]. The slowly varying envelope of a data frame in a normal dispersion fiber corresponds to the refractive index profile of a fiber Bragg grating:

- A fiber Bragg grating with large value of the refractive index. This is equivalent to a waveform with large optical power launched in an optical fiber with normal dispersion.
- A wide fiber Bragg grating. This corresponds to a waveform with a long duration launched in an optical fiber with normal dispersion.

In both of the cases described above, the larger the refractive index of the fiber grating and/or the larger the fiber grating length, the closer to the maximum value of 1 the reflectance of the fiber grating will be over a wide spectral range. Likewise, in both of these cases, the narrower will be the frequency bands whose reflectance is significantly lower than 1, since constructive interference in the forward direction would take place in a narrow bands that decrease with both the refractive index of fiber the grading and the fiber grading width. Therefore, the reflection spectra of the waveform launched in the corresponding optical fiber would also be close to 1 over a wide range of the eigenvalue ζ and the reflection spectra will be different from 1 in narrow eigenvalue bands whose widths decrease with the launch power and waveform duration at the transmitter. As a consequence, higher launch powers and a larger number of symbols per data frame require higher reflection spectra resolution.

The numerical error due to the Born approximation also increases with the the average power, since the error per time step increases. Moreover, a larger number of symbols in the frame implies that more iterations are needed in the INFT algorithms, and the errors will accumulate due to the Born approximation. The combination of the finite reflection spectra resolution in the NFT algorithms and the Born approximation in the INFT algorithms leads to the exponential increase in the errors with both the average power and the number of symbols per data frame as shown in Figs. 2.5 and 2.7.

2.5. Conclusion

This research used computationally efficient and robust computational methods to implement the NFT-INFT algorithms that work well when the reflection spectra is close to 1. It investigated the computational cost of nonlinear compensation techniques based on the NFT applied to optical transmission systems with normal dispersion fibers. The QPSK format was used with raised cosine spectral characteristic to show that the computational cost of the NFT-INFT algorithms increases exponentially or faster with both the channel power and with the number of

symbols per data frame. It is shown that the computational cost of the NFT is primarily limited by two factors: 1) The eigenvalue resolution required for the reflection spectra in the NFT and 2) The number of samples per symbol required to satisfy the Born approximation in the INFT. Since the computational NFT methods that were investigated require that the slowly varying envelope of the optical signal converges towards zero before the edges of the simulation window, the relative guard time has to be increased beyond $t_{g,R} = 1.2$ at higher power levels due to the increase in the spectral bandwidth along the propagation due to the fiber nonlinearity. This is a third, additional, effect that contributes to the decrease of the effectiveness of the NFT as a technique for nonlinear mitigation.

The computational error of the NFT due to the finite eigenvalue resolution of the reflection spectra is the result of an intrinsic property of the ZSSP, since the reflection spectra have to be able to reconstruct the waveform at any position z along the direction of propagation up to the point in which the nonlinear effect does not cause additional changes in the Fourier spectrum. That distance can be orders of magnitude larger than the actual transmission distance when the optical fiber is operating in the nonlinear regime. If this condition is not satisfied, the computational error of the NFT-INFT algorithms will be large at any point along the transmission. For example, to use the NFT to process the signal that consists of 128 QPSK symbols at 56 GBd per data frame at -8.9 dBm of channel power, whose left reflection spectrum is shown in Fig. 2.2, the NFT requires only 2^{10} points to achieve $Q > 15$ dB. When the channel power is increased to -2.9 dBm, the number of points required by the NFT to achieve $Q > 15$ dB for the same QPSK waveform increases to 2^{17}. For this system to operate at $Q > 15$ dB at 3 dBm, it is estimated that the reflection spectra has to be discretized with at least 2^{103} points to process each QPSK frame with 512 symbols. The associated computational cost is not practical with currently available technology.

This study only explores data modulation in the time domain using the QPSK raised cosine modulation format. Le, et al. [28], carried out a study in which the signal was modulated directly in the left reflection spectrum in a transmission system that consisted of anomalous dispersion fibers. In that study, the peak performance was observed at only -4 dBm of average power per data frame, which was 3 dB above the peak performance of -7 dBm of average power per data frame produced by modulation in the time domain. Because of the guard time requirement due to the chromatic dispersion after $2,000$ km of propagation distance, the actual channel power for

peak performance in those two cases are -13.3 dBm and -16.6 dBm, respectively. Additional studies need to be carried out to determine the effectiveness of directly modulating the left- or the right-reflection spectrum. With all the results presented here it is expected that extending this method to normal dispersion fibers is challenging. Systems with -2.9 dBm channel power, which corresponds to 0 dBm of average power per data frame with 128 symbols per data frame, in the normal dispersion regime have reflection spectra whose magnitudes are within 10^{-10} of 1 over a large portion of the reflection spectra. In the case considered in this study, in which it directly modulated the slowly varying envelope of the optical signal, the maximum magnitude of the reflection spectra magnitude comes so close to 1 that it exceeds the accuracy of the floating point numerical representation at -1.2 dBm of channel power, which corresponds to 1.7 dBm of average power per data frame with 128 symbols per data frame, regardless of the number of points used to discretize the reflection spectra. While the results apply to a particular data format, it is expected that the rapid increase of the required spectral resolution of the NFT algorithms with both the length of the data frame and the average power per data frame will hold generally. The corresponding increase in the computational cost is not dependent on the computational complexity of the NFT and INFT algorithms that are used. These issues should be addressed when assessing the practicality of the NFT with any modulation format.

3. ANOMALOUS DISPERSION REGIME: DISCRETE SPECTRUM

3.1. Background

The spectral efficiency of traditional optical fiber communications systems is limited by the maximum launch power imposed by the Kerr nonlinearity [16]. It is of paramount importance to investigate techniques that have the potential to increase the maximum power and, therefore, the spectral efficiency to increase the data rate that can be transmitted in the optical fiber using the currently available optical fiber transmission links.

An alternative to the traditional linear systems is to use the NFT, also known as forward scattering transform, to exploit the use of the nonlinear spectrum. The NFT is based on the Zakharov-Shabat spectral problem [48]. The NFT provides a solution to the Nonlinear Schrodinger Equation (NLS) which describes the propagation on a lossless and noiseless optical transmission medium. The NFT transforms a waveform into a spectrum function that evolves linearly along an optical fiber in the presence of the nonlinear Kerr effect. Unlike the the conventional Fourier transform, the NFT separates the spectrum into two parts: a continuous and a discrete spectrum. The use of the continuous and the discrete spectra, which evolve linear along the propagation direction, can lead to the development of a modulation format that has the potential to mitigate for the nonlinear impairments and lead to systems with higher spectral efficiencies (SE).

Previous chapter studied the use of one-step digital back-propagation based on the NFT to mitigate the nonlinear Kerr effect in optical fiber communications systems [31]. It was found that the computational cost of this approach becomes unacceptably large at such small data frames and power levels that this method is not practical with the currently available NFT methods. This chapter complements that study by investigating the effectiveness of discrete spectrum modulation.

Discrete spectrum modulation has been investigated in the past as part of eigenvalue communication by [25]. independent groups have brought attention to this approach by proposing modulation formats that use the discrete spectrum of the ZSSP to exploit the potential of this method as a candidate to improve the current capacity of optical fiber system [11][15][24][22].

The method used by Dong *et al.* in [15] and Hari *et al.* in [24] can be described as a type of on-off-keying (OOK) modulation format of multiple eigenvalues. Those methods utilize symbols defined by different combinations of eigenvalues, generating a variety of solitons of different orders. In [24], the authors performed a fine selection of symbols formed with combinations of up to 5 eigenvalues out of 50, choosing only the pulses/symbols that meet a specific pulse duration and bandwidth. This method has achieved SE of 3.14 bits/s/Hz.Even though that method does not encode information on the phase of the discrete spectrum, it does set the adjacent solitons to be as out of phase as possible at the transmitter. Moreover, the SE was calculated at the transmitter. Therefore, it does not take into consideration any change on the pulse duration nor bandwidth. This can only be done when the dispersion length (L_{disp}) is much larger than the system length, which significantly limits the maximum launch power used in this system.

$$L_{disp} = \frac{2\pi c}{\lambda^2}\frac{T_0^2}{D}, \quad L_{period} = \frac{\pi}{2}L_{disp} \tag{3.1}$$

The equation 3.1 shows the relationship of the soliton period and the dispersion length, where T_0 is the basic normalized time, D is the dispersion in ps/(nm×km).

Another modulation technique used in [11] consists of modulating the phase of the discrete spectrum. In that case, a second-order soliton was chosen and two independent quadrature phase-shift keying (QPSK) channels are modulated in each eigenvalue. That method utilizes more degrees of freedom but still presents an unacceptably low SE: it can only achieved 0.12 bits/s/Hz at the receiver.

This section investigates the effectiveness of the use of the discrete spectrum of the ZSSP to encode data in optical fiber communications systems with two eigenvalues that was proposed in [11]. It utilizes the concepts of Nonlinear Frequency Division Multiplexed (NFDM) system introduced by Yousefi *et al.* [45][46][47] and the specific transmitter/receiver model used is based on Bülow *et al.*[11]. The transmitter/receiver evaluated is a second-order soliton with QPSK channels modulated independently in each of the two eigenvalues.

This is a simple model system for the assessment of the robustness of modulating the discrete spectrum of the ZSSP with respect to other fiber impairments, including the Raman effect, third-order dispersion, ASE noise from EDFAs, and lumped gain from EDFAs.

Table 3.1. Related Work Spectral Efficiencies

Modulation	SE (bits/s/Hz)	Source
3-soliton OOK	0.04	Experimented in 2015 [15]
2-soliton QPSK	0.12	Experimented in 2016 [11][43]
2-soliton OOK	0.39	Simulated in 2013 [22]
6-soliton OOK	1.5	Simulated in 2013 [22]
5-soliton OOK	3.14	Experimented in 2016 [24]

The Table 3.1 shows the SE for different proposed methods of discrete spectrum modulation, the 2-eigenvlaue QPSK modulation format has a very small SE when compared to most of the other discrete spectrum modulation systems in this table. The SE of the 2-eigenvalue QPSK modulation format can, in principle, be increased by adding more eigenvalues (higher-order soliton) and/or use a more complex quadrature amplitude modulation (QAM) modulation applied to the spectral function of each eigenvalue. However, the increase in the number of eigenvalues has the potential to decrease the robustness of this method with respect to other impairments.

3.2. Modulation Degrees of Freedom

When modulating the discrete spectrum one may use the following degrees of freedom:

- **Imaginary Axis**. The eigenvalues are positive imaginary, (the negative imaginary eigenvalues are a mirror of the positive, so it is not a degree of freedom)(Ex: 0.3j, 0.6j, etc)

  Implications on the time domain: The larger the eigenvalue is, the taller and narrower is the pulse and therefore the peak power is higher.

  Implications on the frequency domain: The larger the eigenvalue is, the wider is its spectrum, as the pulse energy level transitions are steeper.

- **Real Axis**. The eigenvalues are located on the complex plane. (Ex: 1 + 0.3j , -1 + 0.6j, etc)

  Implications on the time domain: the real part causes the pulse to suffer from the fiber dispersion and it will broaden with the distance.

  Implications on the frequency domain: The larger the real part of the eigenvalue is the more distant from the original center frequency the pulse gets. Therefore if multiple eigenvalues are used it will use a broader spectrum.

- **Phase of the spectral function**. Each eigenvalue has a spectrum function associated with it and it can have different phases.

  Implications on the time domain: the phase of different eigenvalues will change how multiple eigenvalues interact with each other and in high order soliton it will define the pulse shape at a specific point of the breathing process.

  Implications on the frequency domain: It does not affect the spectrum much if the whole period spectrum is considered, because all the phases are used in one period.

- **Amplitude of the spectral function**. Each eigenvalue has a spectrum function associated with it and it can have different amplitudes.

  Implications on the time domain: it given by the pulse distance from the center of the symbol window. It is a type of timing jitter, therefore when the time jitter happens the amplitude of the spectral function is deeply disturbed.

  Implications on the frequency domain: It does not affect the spectrum as the pulse shape remains the same.

3.3. Numerical Methods

The slowly-varying envelope of the optical field in a lossless nonlinear medium including both the second-order and the third-order dispersion described by the NLS [3][9][4]:

$$i\frac{\partial A(t)}{\partial z} + i\frac{\alpha(z)}{2} - \frac{\beta_2}{2}\frac{\partial^2 A(t)}{\partial t^2} - i\frac{\beta_3}{6}\frac{\partial^3 A(t)}{\partial t^3} + \gamma\left|A(t)\right|^2 A(t) = 0, \tag{3.2}$$

The fiber parameters β_2, β_3 and γ are the chromatic dispersion, third-order dispersion and the nonlinearity coefficient, respectively. For the fiber parameters, simulation used an SMF with attenuation $\alpha = 0.2$ dB/km, $\beta_2 = -5.75$ ps^2/km, $\beta_3 = 0.7$ ps^3/km and $\gamma = 1.6$ (W.km)$^{-1}$. The simulated fiber transmission system consists of a dispersion map span of 80 km and propagation distances up to 1600 km.The Raman effect is another nonlinear phenomenon that affects the propagation of the optical signal that is not included in the NSE. The ZSSP does not account for third-order dispersion, fiber losses, and the Raman effect.

The NFT of the signal results is two spectral components: the discrete and the continuous. The discrete spectrum corresponds to the solitonic component of the signal, therefore soliton waves

are generated when a waveform is generated from discrete spectrum of the ZSSP. The eigenvalues ζ_j of the discrete spectrum are located in the complex plane with spectral function $q_d(\zeta_j)$, which is also a complex number [45].

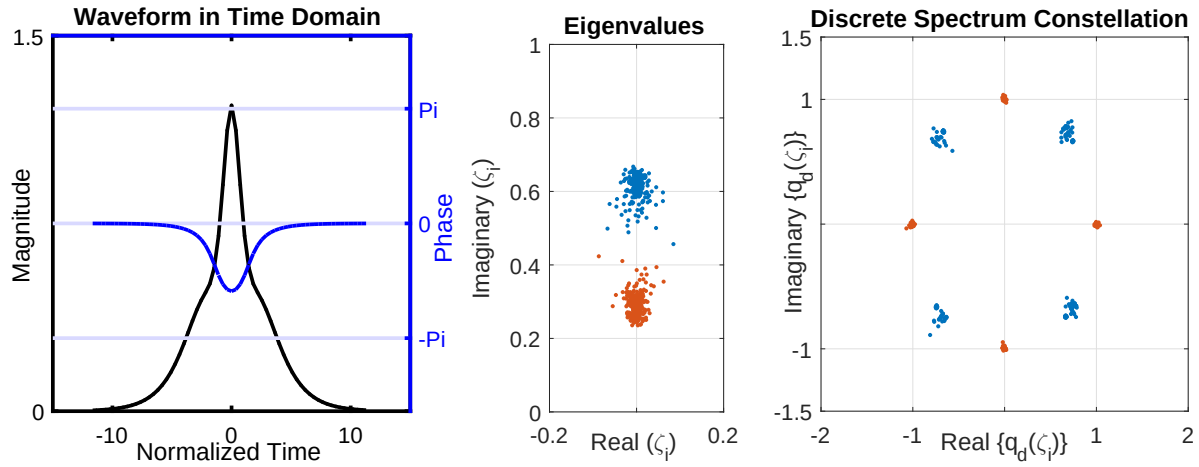

Figure 3.1. On the left: the waveform for a single symbol. In the middle: a constellation diagram of the decoded eigenvalues. The blue dots correspond to the eigenvalue $\zeta_1 = 0.6j$ and the red dots correspond to the eigenvalue $\zeta_2 = 0.3j$. The data is encoded at the spectrum phase of each eigenvalue and it generate another constellation of 16 possible symbols. On the right: the discrete spectrum amplitude and phase constellation associated with each decoded eigenvalue ζ_i.

For this study the simulated system considered only eigenvalues ζ_j on the imaginary axis and with that generate the value of the spectral function $q_d(\zeta_j)$ in the complex plane as a QPSK modulation for each eigenvalue. This system used two eigenvalues, $\zeta_1 = 0.6j$ and $\zeta_2 = 0.3j$, to generate the 2-soliton waveform with independent QPSK modulation of each respective spectral function $q_d(\zeta_j)$.

The algorithms for the NFT and its inverse NFT (INFT) are based on the Ablowitz-Ladik and the Darboux transform, respectively. The Ablowitz-Ladik combined with Newton-Raphson method is a suitable NFT method to recover the eigenvalues ζ_j and their respective encoded spectral functions $q_d(\zeta_j)$ at the receiver. On the transmitter, the waveform is generated from the eigenvlaues and the spectral functions using the Darboux transform.

The Darboux transform [22] is used to generate the waveform of the specific 2-soliton with the information encoded into the phase of the spectral function associated with each of the two discrete eigenvalues with independent QPSK channels. The waveform in [11] is generated using

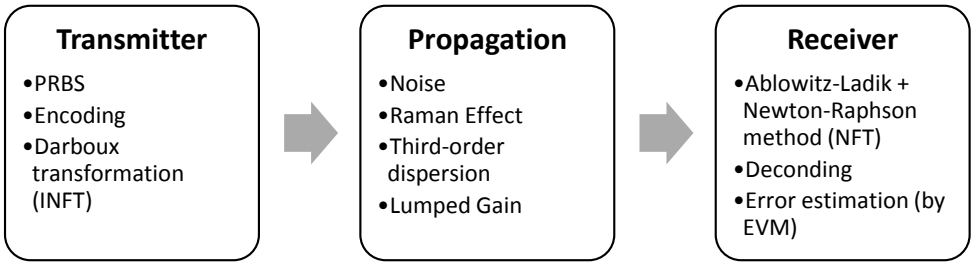

Figure 3.2. Schematic for the simulations.

64 GSa/s and pulse width of 1 ns, which corresponds to therefore 64 samples per symbol, with launch power (average power) of -5.4 dBm and optical filter bandwidth of 33 GHz. In this study, the symbol period, the sampling frequency, and the in-line filter bandwidth are adjusted to according to the specified launch power, maintaining the same proportion.

At the receiver, the signal is up-sampled to 1024 for the symbol period T_{S1} and 2048 for the symbol period T_{S2} ($T_{S2} = 2T_{S1}$), in order to meet the NFT requirements, then the Ablowitz-Ladik method calculates the discrete spectrum of the signal to extract the encoded spectral functions associated to the two eigenvalues used. To extract the eigenvalues that were transmitted without having to scan over a large area, the Ablowitz-Ladik method was combined with the Newton-Ralphson method. The combination of these two methods reduce the computational cost to identify the eigenvalues, which may undergo changes due other effects along the fiber propagation that are not included in the ZSSP. This was the approach used in [11],[8],[10],[24][23],[15].

The Q-factor associated to each eigenvalue is estimated based on the Error Vector Magnitude (EVM) of the received QPSK signal of the received spectral function of each eigenvalue. The EVM is one efficient indicator of the quality of the received signal in systems that use quadrature amplitude modulation that is based on the deviation of the complex value of the received symbol with its ideal location on the complex plane [38]. To calculate the spectral efficiency, the final spectrum bandwidth and the symbol rate at the receiver are considered.

3.4. Results

Each of the fiber impairments were simulated from 200 km to 1600 km of propagation distance on anomalous dispersion fibers with launch power levels from -10 dBm to $+15$ dBm. In all cases the transmitter and receiver used are the same for the same launch power. The pulse

duration and the receiver bandwidth are adjusted to produce the eigenvalues of the ZSSP for each launch power.

3.4.1. Baseline

The Baseline simulation is the simulation obtained with the fiber model without any of the physical impairments of the optical fiber. The ideal optical fiber case is simulated without the following effects: distributed losses, third-order dispersion, ASE noise, and the Raman effect. Because the modulation format contains two individual independent channels, we analyze the Q-factor individually for each channel, as they are associated with different eigenvalues.

Figure 3.3 shows the performance of the baseline simulation as a function of the propagation distance and the launch power over. Figure 3.3(a) shows the Q-factor of the first eigenvalue, $\zeta_1 = 0.6j$, and Figure 3.3(b) shows the Q-factor of the second eigenvalue, $\zeta_2 = 0.3j$.

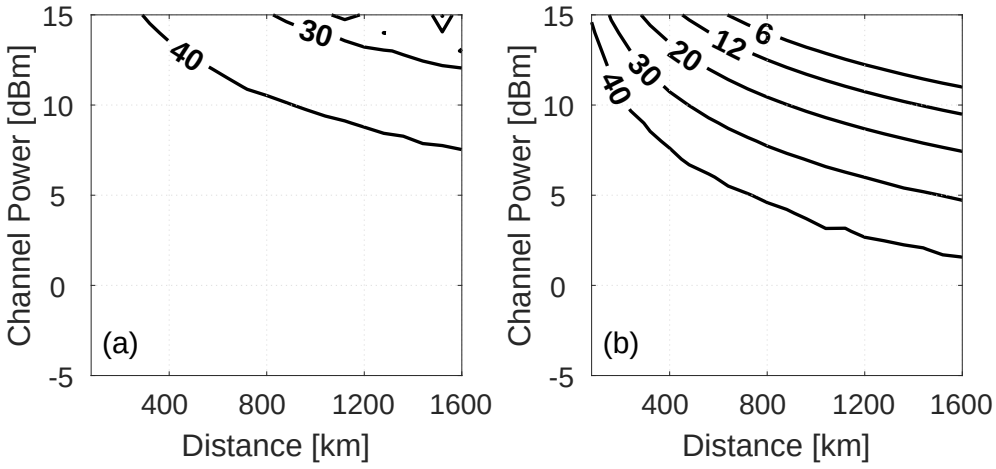

Figure 3.3. Baseline performance of system with QPSK spectrum modulation of the spectral function of two eigenvalues of the ZSSP: (a) shows results for the eigenvalue $\zeta_1 = 0.6j$ and (b) shows results for the eigenvalue $\zeta_2 = 0.3j$. The level curves shown in these two sub-figures are for the following values of the Q-factor: 6, 12, 20, 30 and 40 dB. The area with Q-factor bellow 6 dB represent the unacceptably low Q-factor for a QPSK signal.

In principle, the Q-factor associated to the eigenvalues of the ZSSP should not decay as the signal propagates along an ideal lossless fiber. However even the ideal fiber simulation has presented some distortions at the receiver at long distances. At the upper right corner of Figs. 3.3(a) and (b) we observed the degradation of the Q-factor with the increase of both the launch power and the

propagation distance, which primarily affects the eigenvalue ζ_2. This performance degradation in the ideal fiber model is due to the finite size of the time window used to represent the waveform that leads to inter-symbol interference (ISI).The ISI is caused by the proximity of neighbor symbol and it affects the breathing process of the solitons. This ISI includes the interaction among neighboring solitons described in [20]. As the launch power increases, the soliton breathing period decreases. Therefore, there are more soliton periods in the same propagation distance and it degrades the waveform. To investigate the sources of errors due to the finite size of the time window, this simulations also investigated the same system with twice the symbol period with the same sample rate to maintain the accuracy of the waveform discretization and, consequently, we also doubled the number of points used in the Fast Fourier Transforms (FFT) and the NFT.

3.4.1.1. Mitigating inter-symbol interference

Neighbor symbols may interfere with each other even without the presence of other fiber impairments. To investigate the ISI effect, this section studied the performance of the same system with twice the symbol period. The symbol period denoted as T_{S1} is the symbol period of the system that corresponds to that in [11]m while the system with symbol period $T_{S2} = 2T_{S1}$ corresponds to the same waveform with twice the symbol period but with the same sample rate. Figure. 3.4 compares the systems with these two symbol duration and also different number of points used to discretize the FFT and the NFT methods used in the simulations.

For the system with symbol period(T_{S1}), the Q-factor of the second eigenvalue shown in Figure. 3.4(b) drops below zero before 14 dBm of launch power at 1600 km of propagation distance, while the system with twice the symbol period, T_{S2}, still has the Q-factor close to 45 dB at 14 dBm of launch power. Since the goal is to investigate the impact of each of the non-ideal system impairments, this section studies systems with symbol periods T_{S1} and T_{S2}. This allows us to identify the effects that lead to ISI and those who lead to other forms of performance degradation.

The Q-factor in Figures. 3.4(a) and (b) increases when the symbol period T_S is doubled with the same sample rate at the expense of dropping the SE by half. This performance improvement results from the more accurate representation of the second-order soliton as the symbol period increases, which reduces the ISI from the tails of adjacent symbols. Since there was no noticeable improvement in the performance when the number of points used to discretize the FFT and the NFT was increased, that was not a limiting factor in the performance of the system.

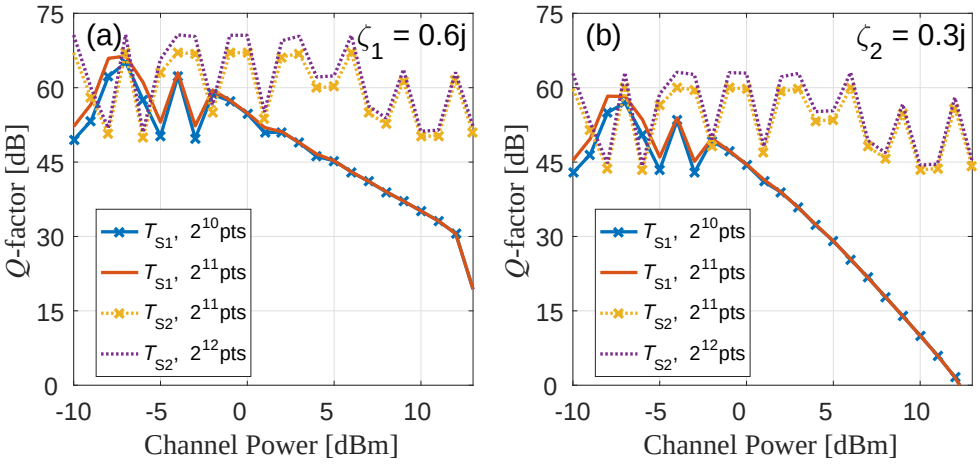

Figure 3.4. Baseline Q-factor as a function of the launch power when the system does not include any effect beyond those included in the ZSSP. (a) Results of signal decoded from the first eigenvalue $\zeta_1 = 0.6j$. (b) Results of signal decoded from the second eigenvalue $\zeta_2 = 0.3j$. Results are shown for the system with symbol period is equal to T_{S1} and for the system with symbol period equal to $T_{S2} = 2T_{S1}$.

3.4.1.2. Constellation analysis

Figures 3.5(a)-(d) show the impact of ISI on the waveform and on the decoded QPSK signal. The waveform is selected from a random symbol from the received sequence at 1600 km with launch power 11 dBm. The results shown in Figures. 3.5 (a, b, c) use $T_S = T_{S1}$ and the results shown in Figures. 3.5 (d, e, f) use $T_S = T_{S2}$.

Figure 3.5(b) shows that there is little distortion on the eigenvalue location after 1600 km of fiber propagation with 11 dBm of launch power. Therefore the eigenvalues were properly recovered at the receiver and robust to cross-talk even using the shorter symbol period T_{S1}. The eigenvalue $\zeta_2 = 0.3j$ experiences more degradation than the eigenvalue $\zeta_1 = 0.6j$ because the portion of the waveform more closely related to the eigenvalue ζ_2 is significantly broader than the portion of the waveform associated to ζ_1. For this reason, the eigenvalue $\zeta_2 = 0.3j$ is more susceptible to suffer from ISI than the eigenvalue $\zeta_1 = 0.6j$ when the symbol period is reduced. The higher susceptibility to errors of the eigenvalue $\zeta_2 = 0.3j$ is shown in Fig. 3.5(c), in which the constellations of $q_d(\zeta_1)$ (blue) are a significantly less dispersed when compared to the constellations of $q_d(\zeta_2)$ (red).

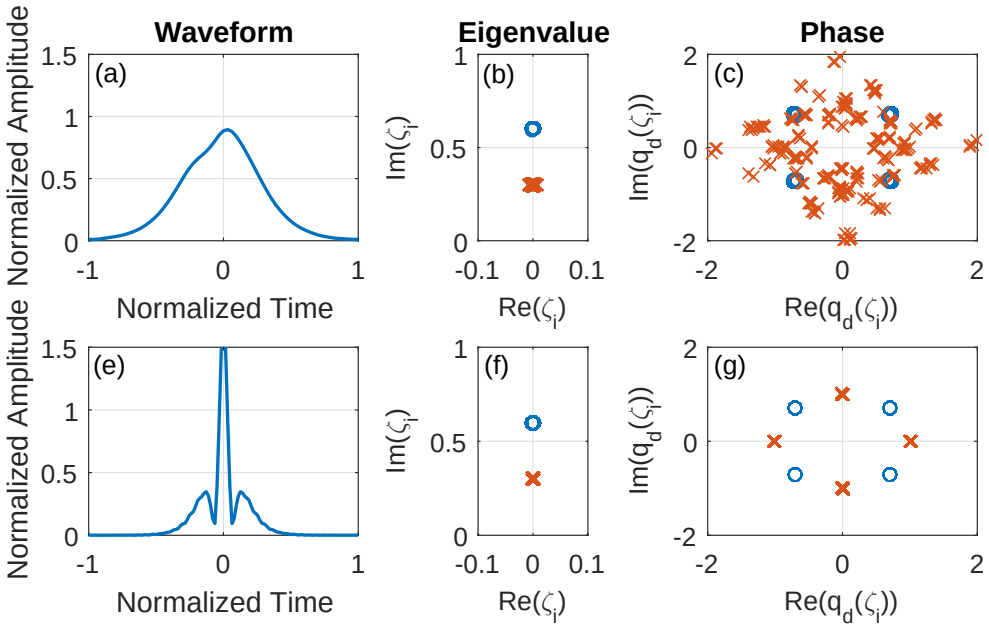

Figure 3.5. Baseline simulation at 1600 km with launch power 11 dBm. (a, b, c) use $T_S = T_{S1}$ while (d, e, f) use $T_S = T_{S2}$. (a, d) Received waveform of one symbol of the sequence. (b, e) Received eigenvalue. (c, f) Normalized received spectral function evaluated at the two eigenvalues: $q_d(\zeta_1)$ in blue and $q_d(\zeta_2)$ in red.

3.4.2. Raman Effect

Figure 3.6 shows how the Raman effect limits the launch power of a system with 1600 km of propagation distance. This study does not include any other effect; it does not include the third-order dispersion, ASE noise, loss and lumped gain along the fiber propagation. Since that ISI plays an important rule on the performance of this system for launch power levels above 10 dBm at the 1600 km of propagation distance, simulations obtained results with the symbol period equal to T_{S1} and T_{S2}.

The case with regular symbol period, T_{S1}, which corresponds to that in [11], and with doubled symbol period, T_{S2}, is compared versus their corresponding baseline cases. It is not clearly identified the impact of the Raman effect on the the results with the symbol period equal to T_{S1}, since the baseline performance of the signal encoded in the eigenvalue $\zeta_2 = 0.3j$ degrades rapidly with the launch power. However, when the symbol period is equal to T_{S2}, the Raman effect limit the performance of the system to launch power levels below 11 dBm.

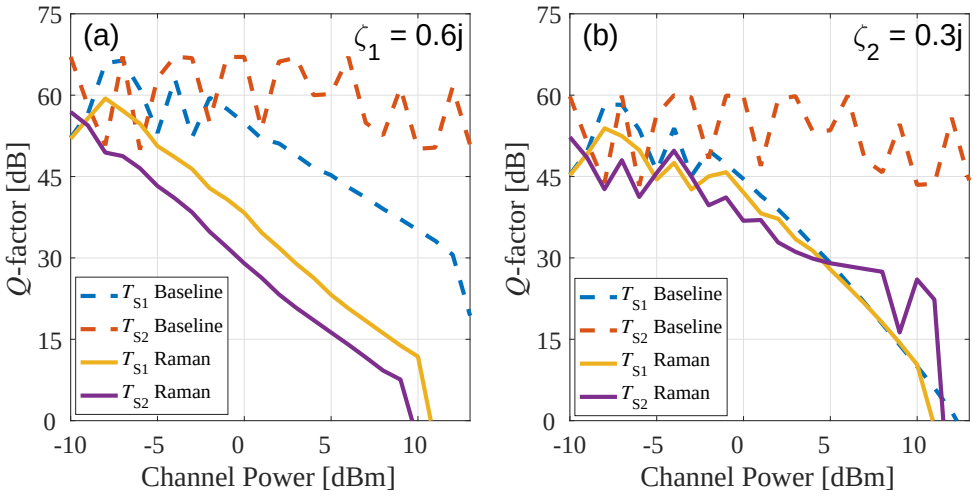

Figure 3.6. Q-factor as a function of the launch power when the system includes only the Raman effect. (a) Results of signal decoded from the first eigenvalue $\zeta_1 = 0.6j$. (b) Results of signal decoded from the second eigenvalue $\zeta_2 = 0.3j$.; Results are shown for the system with symbol period is equal to T_{S1} and for the system with symbol period equal to $T_{S2} = 2T_{S1}$.

The system with the smaller symbol period T_{S1} appears to outperform the larger symbol period T_{S12} in the results shown in Fig. 3.6(a). However, that performance difference is the result of the use of the launch power, which implies that the simulation with symbol period T_{S2} needs to have twice the peak power of the simulation with T_{S1} to correspond to the same launch power.

3.4.2.1. Constellation analysis

Since this coding scheme generates a second-order soliton, the portion of the waveform associated to each individual eigenvalue may propagate with different group velocity when subjected to the fiber impairments, such as the Raman effects. The Raman effects disturb the equilibrium of the interaction forces of the given second-order soliton. As it is composed by two eigenvalues of the ZSSP, the unbalancing of the attraction and repulsing forces cause pulse displacements, resulting in the second-order soliton breaking apart into 2 individual solitons [21][26].

When the propagation distance is long enough or the launch power is high enough, the the main lobe of one of the two soliton components reach the neighboring symbol due to the Raman effect. Once that happens, the ISI due to Raman lead to errors in the symbol decoding. This is caused by the attracting and repealing forces of the solitons main lobe to the neighbor symbol. Before the total collapse of this modulation scheme due to ISI, the pulse shift inside the symbol

time window due to the Raman effect causes changes in the amplitude of the spectral function $q(\zeta)$ of at least one of the eigenvalues. This change in the amplitude of $q(\zeta)$, which increases linearly with the propagation distance until the onset of ISI, precludes the use of QAM with multiple levels of modulation and, thus, significantly limiting the possibility of increase in the SE with the use of multilevel modulation. The larger shift in the amplitude of the spectral functions for the case in which the symbol period is equal to T_{S2} compared to that in which the symbol period is equal to T_{S1} is because the former system with larger symbol period has a higher peak power for the same launch power.

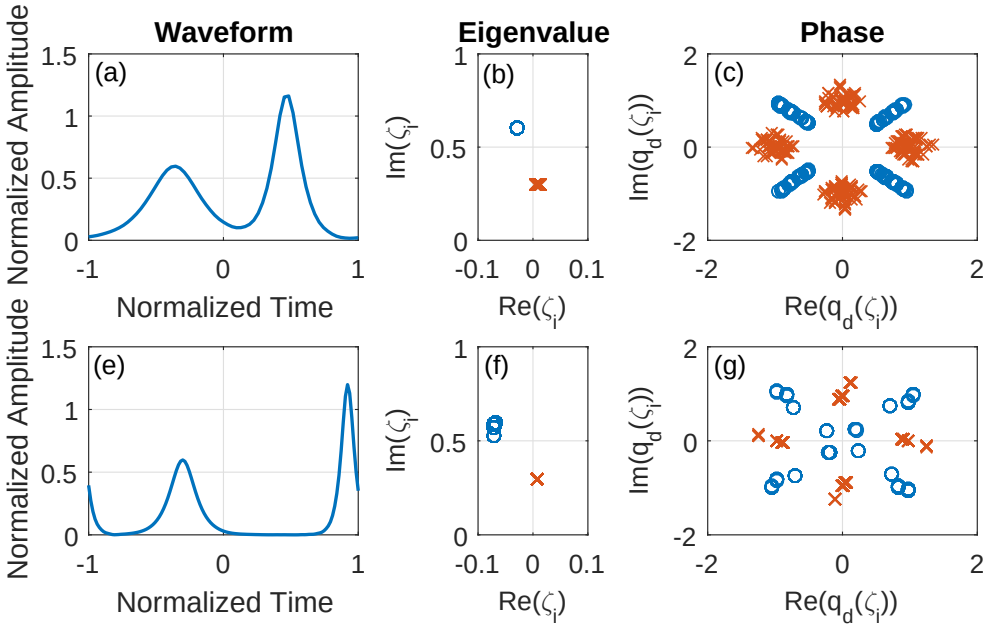

Figure 3.7. Simulation with the Raman effect at 1600 km with 9 dBm of launch power. (a,b,c) Shows results for the symbol period T_{S1}. (d,e,f) Shows results for the symbol period T_{S2}. (a,d) Received waveform of one symbol of the sequence. (b,e) Received eigenvalue. (c,f) Normalized received spectral function constellations, $q_d(\zeta_1)$ in blue and $q_d(\zeta_2)$ in red.

The changes in the value of the eigenvalues due to the Raman effect do not make them to cross the threshold of inter-eigenvalue interference at the propagation distance and launch powers that we considered, but the Raman effect significantly changes the eigenvalue ζ_1 from its original value $0.6j$. This suggests that the Raman effect would significantly limit the performance of modu-

lation schemes in which the information is encoded in the location of the eigenvalues in the complex plane.

Note, however, that most of the shift in the spectral function of the eigenvalues $q(\zeta)$ is deterministic and could be taken into account when designing the symbols to optimize the choice of the magnitude and the phase, as long as this shift is not large enough to lead to decoding errors due to ISI.

The constellations of $q_d(\zeta_1)$ shown in blue in Fig. 3.7(c) maintain approximately same phase for $\zeta_1 = 0.6j$ but have different amplitudes due to the Raman effect, depending on the symbol pattern. The 16 different symbols have four starting patterns determined by the phase difference between the two soliton components. This phase difference determines the shape of the waveform at the starting point of the breathing period. Appendix A.1 addresses how one can recognize these patterns and how one can mitigate for those deterministic shifts in the amplitude of the phase function before the onset of decoding errors due to ISI.

Differently from the constellations of $q_d(\zeta_1)$, the constellations of $q_d(\zeta_2)$ shown in red in Figure. 3.7(c) are spread equally on amplitude and phase, this is because at this propagation distance and channel power, the ISI (present on the baseline simulation) is the primary cause of the distortions in $q_d(\zeta_2)$.

For the system with symbol period T_{S2}, in which ISI is virtually absent, both $q_d(\zeta_1)$ and $q_d(\zeta_2)$ constellations are distorted by the Raman effect, even though $q_d(\zeta_1)$ is more strongly affected by the Raman effect than $q_d(\zeta_2)$ because the former is related to a soliton wave with a much higher peak power when compared to the latter.

3.4.3. Third-Order Dispersion

The impact of third-order dispersion in the eigenvalue encoding is also investigated with the two different symbol periods T_{S1} and T_{S2}. Figure 3.8 shows the impact of third-order dispersion as the power increases. For the T_{S2} the impact on the Q-factor estimation at a launch power of 12 dBm is of approximately 40 dB when compared to the baseline simulation without any fiber impairments. Therefore, the third-order dispersion alone can cause the communication system with 1600 km to fail at launch powers higher than 13 dBm. The performance degradation due to third-order dispersion of the eigenvalue encoding based on the ZSSP with the increase in the launch

power is due to the bandwidth increase required to generate the second-order soliton as the launch power increases.

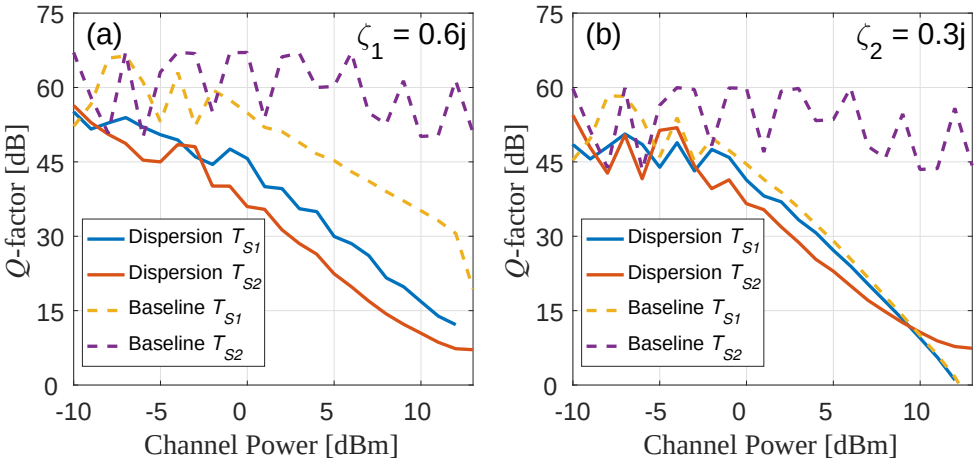

Figure 3.8. Q-factor as a function of the launch power when third-order dispersion is included. (a) Results of signal decoded from the first eigenvalue $\zeta_1 = 0.6j$. (b) Results of signal decoded from the second eigenvalue $\zeta_2 = 0.3j$. Results are shown for the system with symbol period is equal to T_{S1} and for the system with symbol period equal to $T_{S2} = 2T_{S1}$.

3.4.3.1. Constellation analysis

To study how the third-order dispersion impact the signal a constellation and pulse shape analysis was made on figure 3.9. It shows that the eigenvalues location does not suffer degradation at 12 dBm of launch power after 1600 km of propagation distance. However, the spectral function constellations undergo a significant pattern of spread, which causes the Q-factor to degrade significantly.

3.4.4. Lumped Gain

To address the impact of the lumped gain from EDFAs, it is necessary to adjust the launched waveform because the effective nonlinearity of the fiber is lower than that of a lossless fiber with the same launch power. This occurs because the average power of the waveform decreases as the waveform propagates through a practical fiber with losses. One approach to mitigate the effect of losses is to calculate an average/effective value of the nonlinear coefficient of the fiber and generate the waveform based on that new effective nonlinearity coefficient. Calculations show that a launch

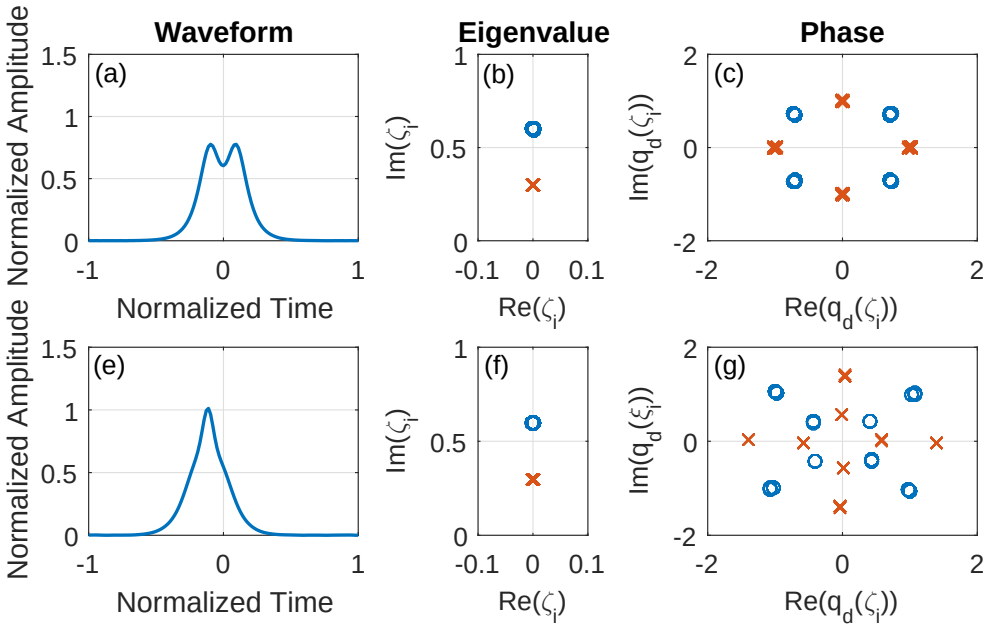

Figure 3.9. Third-order dispersion simulation results with symbol period equal to T_{S2} at 1600 km of propagation distance. (a,b,c) Results with launch power 1 dBm. (d,e,f) Results with launch power 12 dBm. (a,d) Received waveform of one symbol of the sequence. (b,e) Received eigenvalue. (c,f) Normalized Received spectral function constellations, $q_d(\zeta_1)$ in blue and $q_d(\zeta_2)$ in red.

power increase of about 5.7 dB is needed for a 80 km fiber span with attenuation of of 0.2 dB/km when compared to the ideal lossless fiber. This is the same technique used in [24],[11].

The results shown in Figure. 3.10 with fiber losses and lumped gain from EDFAs show a significant degradation of the Q-factor with the increase of the launch power. This is caused by the worsening of the approximation between the lossless fiber approximation and the practical fiber with losses and lumped gain, at the end of each span, with the increase of the local power variation from the beginning to the end of a fiber span. This effect is also symbol dependent and the error is much larger for specific symbols, especially those with large peak-to-average power ratio (PAPR).

3.4.4.1. Constellation analysis

Because the performance with fiber losses and lumped gain from EDFAs decreases so rapidly with the increase of the launch power, I examined the effect of fiber losses and lumped gain in the waveform generated by a symbol that was strongly affected by fiber losses and lumped gain. Figure 3.11 shows results for -0.25 dBm of launch power when fiber losses and lumped gain are included. The constellations for both simulations with symbol period T_{S1} and symbol period T_{S2} are almost equally affected because the waveform degradation is not due to ISI. The eigenvalues

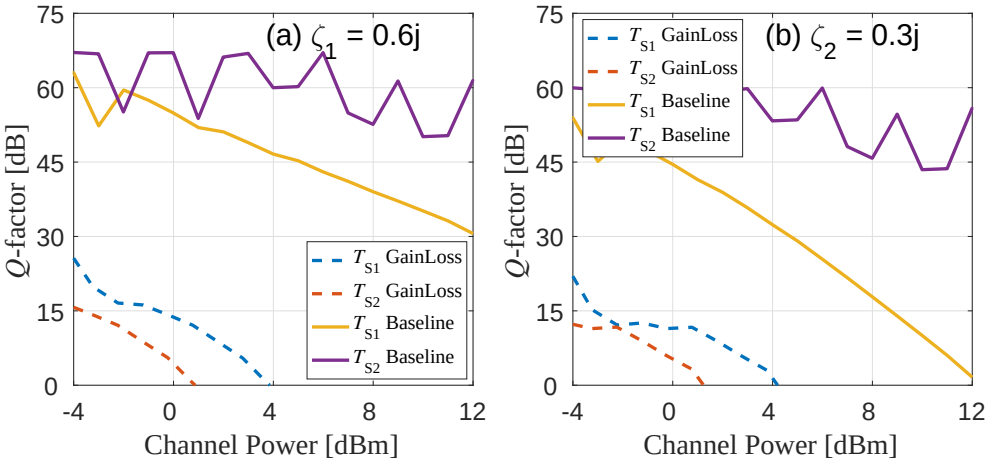

Figure 3.10. Q-factor as a function of the launch power when the system includes only losses and lumped gain from EDFAs. (a) Results of signal decoded from the first eigenvalue $\zeta_1 = 0.6j$. (b) Results of signal decoded from the second eigenvalue $\zeta_2 = 0.3j$. Results are shown for the system with symbol period is equal to T_{S1} and for the system with symbol period equal to $T_{S2} = 2T_{S1}$.

shown in Figures. 3.11 (b,e) are disturbed even at -0.25 dBm of launch power, while the $q_d(\zeta_j)$ constellations are significantly spread out, reducing the Q-factors down to 10 dB at this low launch power.

Due to errors in the decoding of some of the transmitted symbols using discrete spectrum modulation, Bülow proposed to drop the symbols that are more prone to errors in [11]. After dropping 25% the symbols with errors and calculating the Q-factor for the remaining symbols, a significant improvement in the Q-factor was observed at the expense of a reduction of 25% in the SE. When all the symbols are included, the Q-factor is equal to 1 dB due to the large value of the EVM associated to a few of the symbols. When the 25% of the symbols with the largest EVM are excluded, the Q-factor increases to 13 dBm. Therefore, to mitigate the errors due to losses and lumped amplification, the symbols with the higherst EVM, which correspond to those with high PAPR, have to be excluded.

One approach to mitigate the impairments due to fiber losses and lumped gain from EDFAs in the discrete spectrum modulation is to use distributed Raman amplification. However, the high cost and the low efficiency of that amplification scheme significantly limit the use of that method to enhance the effectiveness of discrete spectrum modulation based on the ZSSP.

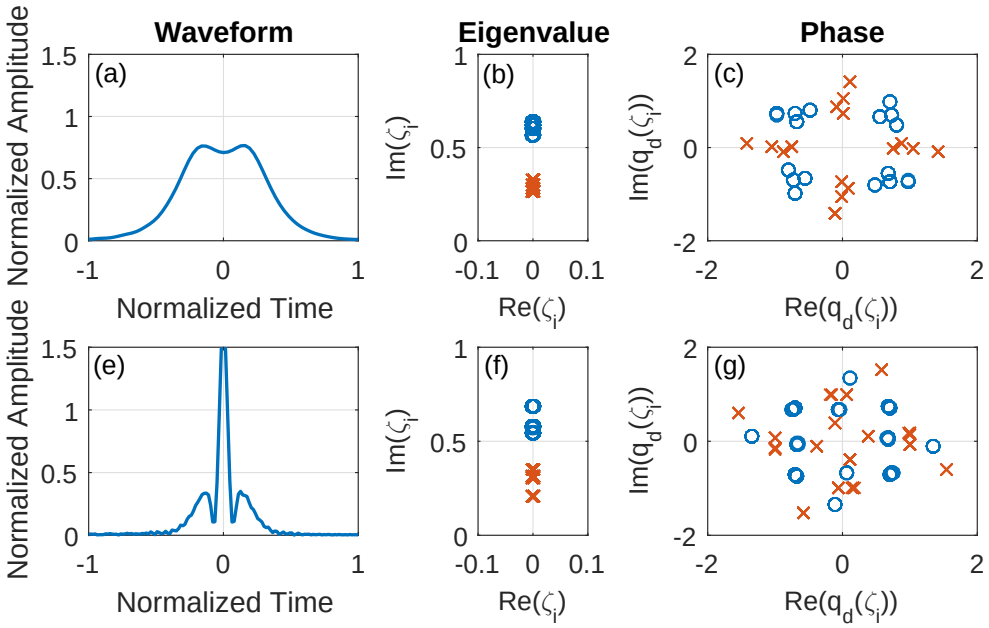

Figure 3.11. Simulation results at 1600 km or propagation distance with launch power −0.25 dBm. (a,b,c) Results with symbol period equal to T_{S1}. (d,e,f) Results with symbol period equal to T_{S2}. (a,d) Received waveform of one symbol of the sequence. (b,e) Received eigenvalue. (c,f) Normalized Received spectral function constellations, $q_d(\zeta_1)$ in blue and $q_d(\zeta_2)$ in red.

3.4.5. ASE Noise

This sub-section investigates the impact of the ASE noise in the performance of discrete spectrum modulation. This system consists of 20 spans of 80 km with an EDFA at the end of each span. Since the purpose of this study is to characterize the impact of optical noise in the performance of eigenvalue modulation, the launch power is maintained constant throughout the propagation, but ASE noise is added at the end of each span consistently with the amount of ASE noise that is generated in a fiber transmission system with losses and lumped amplification by EDFAs. To limit the noise bandwidth, the system used an optical filter with 33 GHz of bandwidth for the pulse with $T_{S1} = 1$ ns to limit the ASE noise.

Figure 3.12 shows the Q-factor as a function of the launch power for both eigenvalues and for symbol periods equal to T_{S1} and T_{S2}. The ASE noise limits the maximum power that can be launched in the two-eigenvalue system. The signal encoded in the spectral function of the eigenvalue ζ_1 is limited to about 0 dBm of launch power. At low channel power levels, the ASE limits the performance because the noise dominates the signal. As the channel power increases, the nonlinear

noise increases faster than the signal for at about -7 dBm for $\zeta_1 = 0.6j$ and 0 dBm for $\zeta_2 = 0.3j$ because of the high PAPR of the second-order solitons.

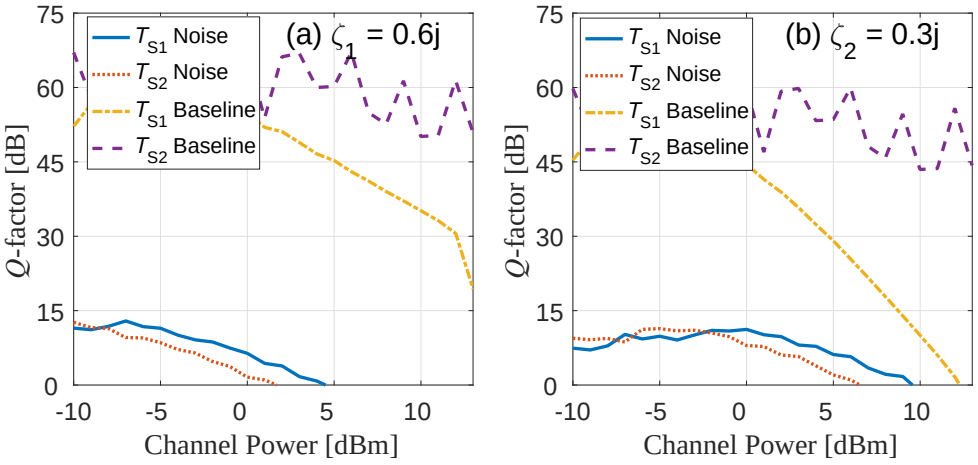

Figure 3.12. Q-factor as a function of the launch power when the system includes only ASE noise from EDFAs. (a) Results of signal decoded from the first eigenvalue $\zeta_1 = 0.6j$. (b) Results of signal decoded from the second eigenvalue $\zeta_2 = 0.3j$.

3.4.6. All Impairments Combined

When all the impairments are considered, the performance is capped by the combination of all these effects. However the lumped gain in EDFAs to compensate for the fiber losses along the transmission dominates the overall performance degradation. As discussed in Sec. 3.4.4, this performance degradation with the increase of the launch power is due to the degradation of the lossless propagation approximation modeled by the ZSSP compared with the practical model that accounts for losses and lumped amplification from EDFAs located at the end of each fiber span. In essence, the distributed losses have the effect of changing the local eigenvalues of the ZSSP along the propagation distance, which deviates from those of the lossless propagation model of the ZSSP as the launch power increases.

Figure 3.14 shows the case with T_{S2}, in this case we can see the effects without the cap of the baseline ISI that exists at T_{S1}. Note that the performance with symbol period T_{S2} is 3 dB shifted when compared to that with T_{S1} because the former has twice the symbol period of the latter.

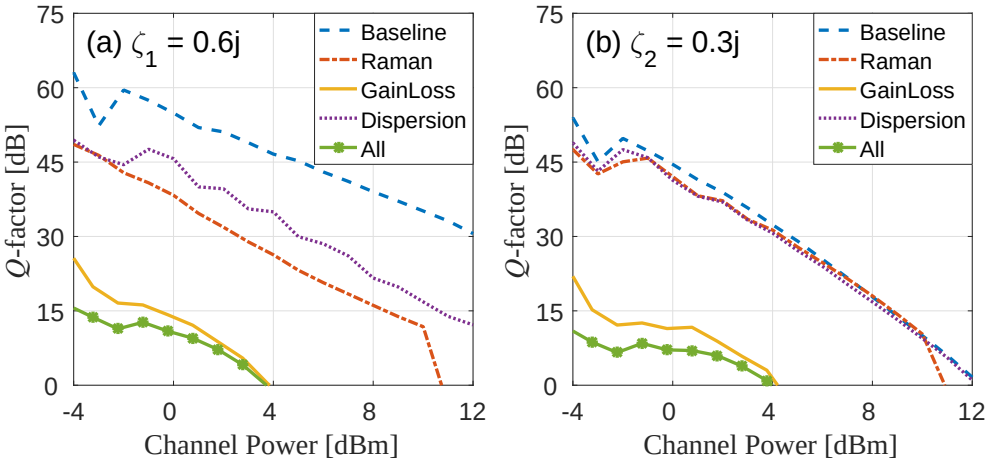

Figure 3.13. Q-factor as a function of the launch power when all the effects are included. (a) Results of signal decoded from the first eigenvalue $\zeta_1 = 0.6j$. (b) Results of signal decoded from the second eigenvalue $\zeta_2 = 0.3j$. Results are shown for the system with symbol period is equal to T_{S1}.

3.4.6.1. Constellation analysis

The impact of all the effects combined have little difference from the case T_{S1} and T_{S2} besides the 3 dB shift caused by the larger window, therefore Figure 3.15 compares the signal constellation and pulse shape from two different power levels, -7 dBm and 0 dBm; this shows the impact of the different launch powers. At a low power the eigenvalues are recovered properly without any kind of displacement while the spectral function constellations show a pattern of spread that causes the Q-factor estimation to decay.

From Figure 3.14 it is possible to conclude that gain and loss along with noise are the dominant impairments at 1600 km propagation with a launch power around 3 dBm. At Figure 3.16 the impact of each impairment is shown in a different plot to clarify the impact at the same original waveform.

3.5. Conclusion

In an ideal lossless fiber without ASE noise, the Raman effect is the limiting factor of the performance of a modulation scheme based on a two-eigenvalue spectrum modulation, since the Raman effect brakes the second-order soliton and at least one of the two soliton components shifts into a neighbor symbol. For this modulation format it occurs when the launch power is higher than 10.25 dBm for a propagation over 1600 km of optical fiber. This degradation due to the Raman

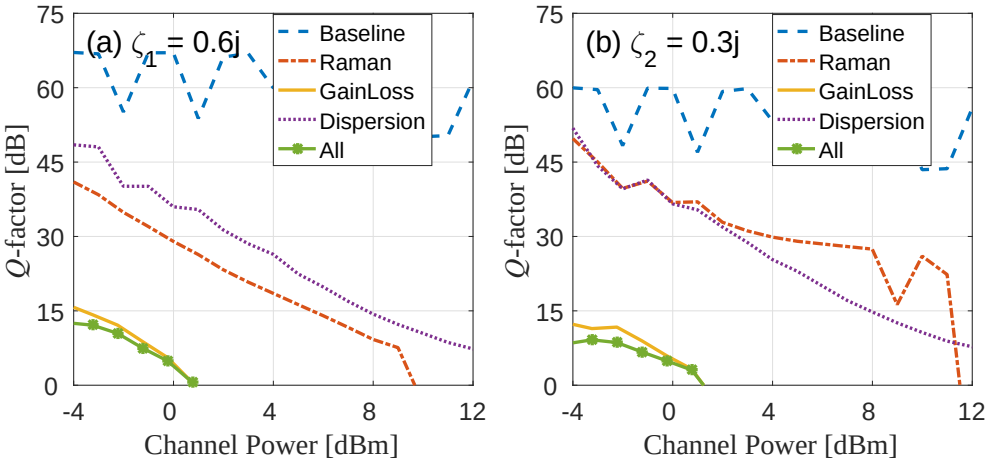

Figure 3.14. Q-factor as a function of the launch power when all the effects are included and the symbol period is equal to $T_{S2} = 2T_{S1}$. (a) Results of signal decoded from the first eigenvalue $\zeta_1 = 0.6j$. (b) Results of signal decoded from the second eigenvalue $\zeta_2 = 0.3j$.

effect under that power level can be compensated through equalizing the signal and mapping each symbol individually to compensate for the Raman shift suffered for the given distance. However, this consequence of the Raman effect significantly limits the use of multilevel modulation formats that could have been used to increase the SE. At even lower launch power levels, other effects such as ASE noise and lumped gain from EDFAs limit this system performance. In the systems that we investigated, the primary limiting factor of the performance was the lumped gain from EDFAs, which limits the maximum launch power to about 2 dBm. The performance degradation of the discrete spectrum modulation format is due to the lumped gain to compensate for the fiber losses, which deviates from the lossless fiber model that is described by the ZSSP. The performance of discrete spectrum modulation is expected to worsen with the increase of the number discrete eigenvalues per symbol. Therefore, the use of modulation of the discrete spectrum of the ZSSP is unlikely to lead to the design of optical fiber communications systems with spectral efficiency higher than those of conventional QAM systems that are currently being used.

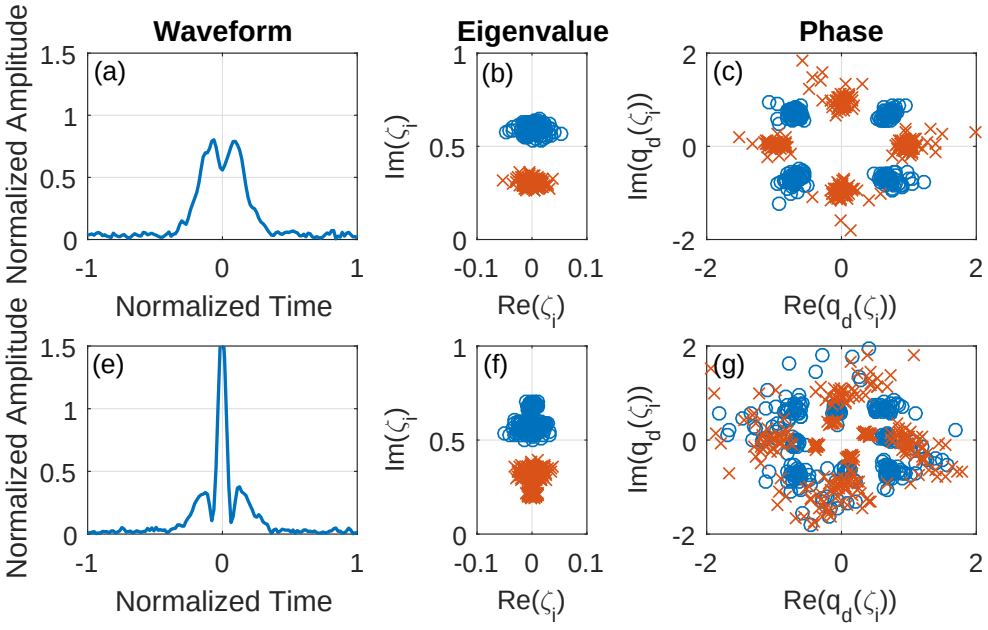

Figure 3.15. All effects simulation results with symbol period equal to T_{S2} at 1600 km of propagation distance. (a,b,c) Results with launch power -7 dBm. (d,e,f) Results with launch power 0 dBm. (a,d) Received waveform of one symbol of the sequence. (b,e) Received eigenvalue. (c,f) Normalized Received spectral function constellations, $q_d(\zeta_1)$ in blue and $q_d(\zeta_2)$ in red.

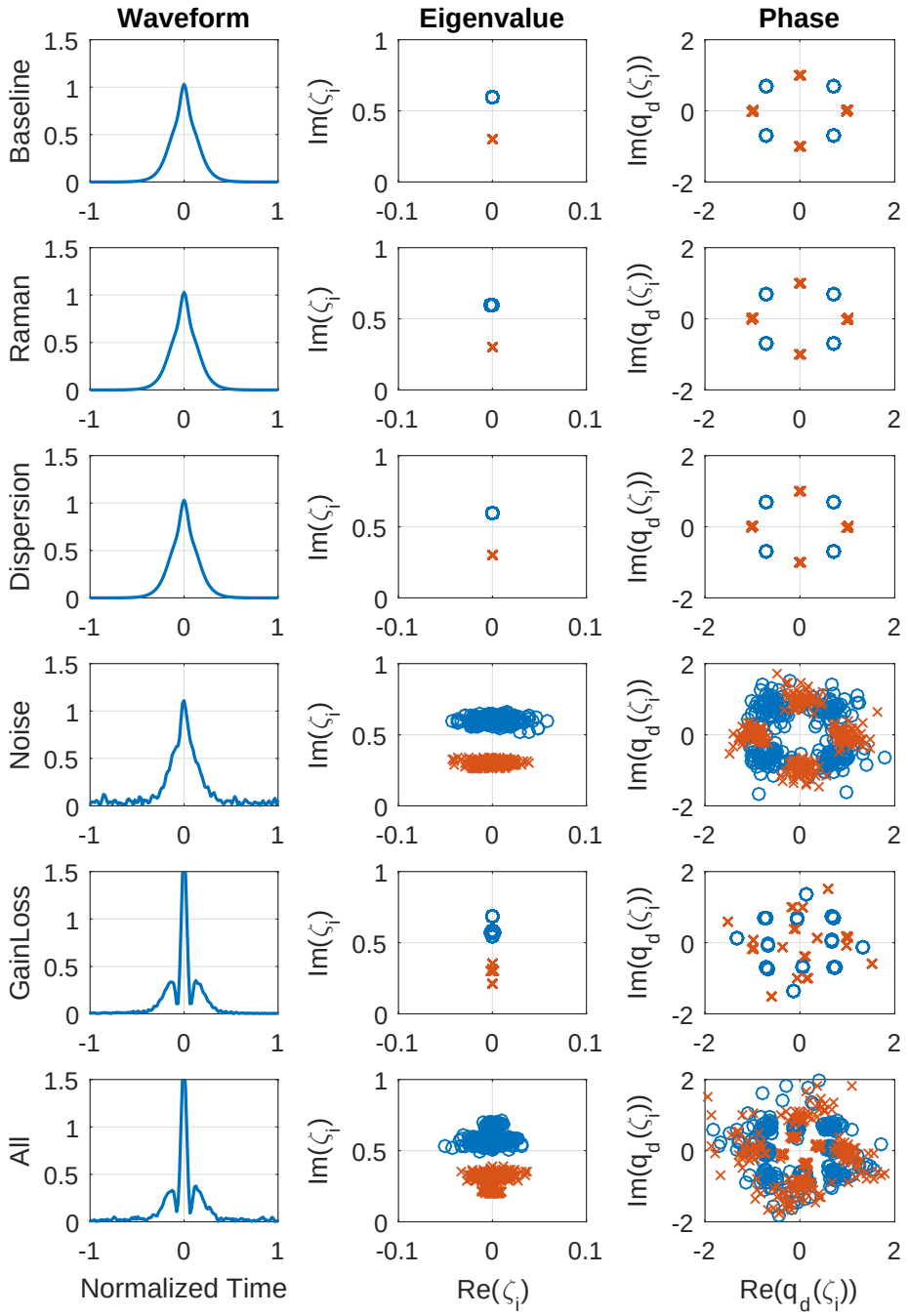

Figure 3.16. All effects simulation results with symbol period equal to T_{S2} at 1600 km of propagation distance. Each row of figures represent a different impairment simulation: Row 1 Baseline, 2 Raman effect, 3 Dispersion, 4 Noise, 5 GainLoss and 6 All impairment. The waveform compared is for the same original symbol and the performance is compared for the same original signal under each of the circumstances. For the Eigenvalue and Phase columns it is used the normalized received spectral function constellations, $q_d(\zeta_1)$ in blue and $q_d(\zeta_2)$ in red.

4. CONCLUSIONS AND RECOMMENDATIONS FOR FUTURE WORK

One of the objectives of this research was to develop a collection of algorithms to build a functional simulation library for optical fiber communication systems, including propagation with ASE noise, loss, gain, Raman and third-order dispersion. Now this platform is available for use in future research projects related to this topic.

On the continuous spectrum at normal dispersion regime it was found that the complexity of the NFT-INFT algorithms exponentially increase as the channel power increases. For the proposed system to operate at $Q > 15$ dB at 3 dBm, it was estimated that the reflection spectra has to be discretized with at least 2^{103} points to process each QPSK frame with 512 symbols. The associated computational cost is not practical with currently available technology. Another trade off is the allocation of a guard time to accommodate for the accumulated dispersion, this way only a fraction of the sent package has effective data, reducing its spectral efficiency. Therefore the use of the NFT continuous spectrum for nonlinear compensation in normal dispersion regime is not a practical method for high launch power with the current NFT-INFT algorithms.

The goal of the second phase of this research was to determine the effectiveness of discrete spectrum modulation using the NFT as a tool to mitigate for the nonlinear Kerr effects that limit the capacity of optical fiber communications systems. The impairments for the 1600 km (20×80 km, with distributed EDFA) of SSMF prevent it to reach channel power levels above 4 dBm for a second-order soliton, which corresponds to only two QPSK wavelength-division multiplexed (WDM) channels. Therefore the use of the discrete spectrum alone on the anomalous regime is not a good candidate for a high spectral efficiency on long distance propagation and high channel power for a second-order soliton.

Even though the NFT methods studied here are not yet practical nor robust to mitigate the nonlinear effects in the normal or in the anomalous dispersion regime using either the continuous or the discrete spectrum of the NFT, more research needs be done with different fiber parameters, different modulation formats and different implementations of the NFT and the INFT algorithms.

REFERENCES

[1] M. J. Ablowitz and J. F. Ladik. Nonlinear differential–difference equations and fourier analysis. *J. Math. Phys.*, 17(6):1011–1018, 1976.

[2] M. J. Ablowitz and H. Segur. *Solitons and the Inverse Scattering Transform*. SIAM, Philadelphia, 1981.

[3] G. P. Agrawal. *Nonlinear Fiber Optics*. Academic Press, San Diego, 3 edition, 2001.

[4] G. P. Agrawal. *Nonlinear Fiber Optics*. Academic Press, San Diego, 4 edition, 2007.

[5] S. Wahls andn H. V. Poor. Fast numerical nonlinear fourier transforms. *IEEE Trans. Info. Theory*, 61(12):6957–6974, 2015.

[6] O. V. Belai, L. L. Frumin, E. V. Podivilov, and D. A. Shapiro. Efficient numerical method of fiber bragg grating synthesis. *J. Opt. Soc. Am. B*, 24(7):1451–1457, 2007.

[7] G. Boffetta and A. R. Osborne. Computation of the direct scattering transform for the nonlinear schodinger equation. *J. Comput. Phys.*, 102:252–264, 1992.

[8] H. Bülow. Experimental assessment of nonlinear fourier transform based detection under fiber nonlinearity. *ECOC*, 2014.

[9] H. Bülow. Experimental demonstration of optical signal detection using nonlinear fourier transform. *J. Lightwave Technol.*, 33(7):1433–1439, 2015.

[10] H. Bülow. Nonlinear fourier transformation based coherent detection scheme for discrete spectrum. *Optical Fiber Communications Conference and Exhibition*, pages 1–3, 2015.

[11] H. Bülow, V. Aref, K. Schuh, and W. Idler. Experimental nonlinear frequency domain equalization of qpsk modulated 2-eigenvalue soliton. *Optical Fiber Communication Conference, OSA Technical Digest*, pages 1–3, 2016.

[12] A. Buryak, J. Bland-Hawthorn, and V. Steblina. Comparison of inverse scattering algorithms for designing ultrabroadband fiber bragg gratings. *Opt. Express*, 17(3):1995–2004, 2009.

[13] K. Chadan and P. C. Sabatier. *Inverse Problems in Quantum Scattering Theory*. Springer, New York, 1977.

[14] Y. Choi, J. Chun, and J. Bae. Numerically extrapolated discrete layer-peeling algorithm for synthesis of nonuniform fiber bragg gratings. *Opt. Express*, 19(9):8254–8266, 2011.

[15] Z. Dong, S. Hari, T. Gui, K. Y. M. I. Zhong, C. Lu, P.-K. A. Wai, F. R. Kschishang, and A. P. T. Lau. Nonlinear frequency division multiplexed based on nft. *IEEE Photon. Tehcnol. Lett.*, 27(15):1621–1623, 2015.

[16] R. J. Essiambre, G. Kramer, P. J. Winzer, G. J. Foschini, and B. Goebel. Capacity limits of optical fiber networks. *Journal of Lightwave Technology*, 28(4):662–701, 2010.

[17] R. J. Essiambre and A. Mecozzi. Capacity limits in single-mode fiber and scaling for spatial multiplexing. In *OFC/NFOEC*, pages 1–3, March 2012.

[18] R. J. Essiambre and R. W. Tkach. Capacity trends and limits of optical communication networks. *Proceedings of the IEEE*, 100(5):1035–1055, May 2012.

[19] R. Feced, M. N. Zervas, and M. A. Muriel. An efficient inverse scattering algorithm for the design of nonuniform fiber bragg gratings. *IEEE J. Quantum Electron.*, 35(8):1105–1115, 1999.

[20] J. P. Gordon. Interaction forces among solitons in optical fibers. *Opt. Lett.*, pages 596–598, 1983.

[21] J. P. Gordon. Theory of the soliton self-frequency shift. *Opt. Lett.*, 11(10):662–664, Oct 1986.

[22] S. Hari, F. Kschischang, and M. Yousefi. Multi-eigenvalue communication via the nonlinear fourier transform. *IEEE International Symposium on Information Theory*, pages 1710–1714, 2013.

[23] S. Hari, F. Kschischang, and M. Yousefi. Multi-eigenvalue communication via the nonlinear fourier transform. *Communications (QBSC)*, pages 92–95, 2014.

[24] S. Hari, M. I. Yousefi, and F. R. Kschischang. Multieigenvalue communication. *Journal of Lightwave Technology*, 34(13):3110–3117, 2016.

[25] A. Hasegawa and Y. Kodama. *Solitonsn in Optical Communications*. Oxford University Press, Oxford, 1995.

[26] A. Hause and F. Mitschke. Soliton trains in motion. *Phys. Rev. A*, 82:043838, Oct 2010.

[27] G. L. Lamb. *Elements of Soliton Theory*. Wiley, New York, 1980.

[28] S. T. Le, J. E. Prilepsky, and S. K. Turitsyn. Nonlinear inverse synthesis for high spectral efficiency transmission in optical fibers. *Opt. Express*, 22(22):26720–26741, 2014.

[29] S. T. Le, J. E. Prilepsky, and S. K. Turitsyn. Nonlinear inverse synthesis technique for optical links with lumbed amplification. *Opt. Express*, 23(7):8317–8325, 2015.

[30] J. Leuthold and W. Freude. *Optical OFDM and Nyquist multiplexing*, volume VIB, chapter 9, pages 381–432. Elsevier, Amsterdan, 6 edition, 2013. An optional note.

[31] I. T. Lima Jr., T. D. S. DeMenezes, V. S. Grigoryan, M. O'Sullivan, and C. R. Menyuk. Nonlinear compensation in optical communication systems with normal dispersion fiber using nonlinear fourier transform (under review). *Journal of Lightwave Technology*, 2016.

[32] I. T. Lima Jr., V. S. Grigoryan, M. O'Sullivan, and C. R. Menyuk. Computational complexity of nonlinear transforms applied to optical communications systems with normal dispersion fibers. In *Proc. of the IEEE Photon. Conf.*, pages 277–278, 2015.

[33] F. L. Mollenauer and J. P. Gordon. *Solitons in optical fibers - Fundamentals and Applications*. Elsevier, Amsterdan, 2006.

[34] J. K. Proakis and M. Salehi. *Fundamentals of Communication Systems*. Pearson, Boston, 2 edition, 2014.

[35] A. Rosenthal and M. Horowitz. Inverse scattering algorithm for reconstructing strongly reflecting fiber bragg gratings. *IEEE J. Quantum Electron.*, 39(8):1018–1026, 2003.

[36] R. Schmogrow, B. Nebendahl, M. Winter, A. Josten, D. Hillerkuss, S. Koenig, J. Meyer, M. Dreschmann, M. Huebner, C. Koos, J. Becker, W. Freude, and J. Leuthold. Corrections to: Error vector magnitude as a performance measure for advanced modulation formats. *IEEE Photon. Technol. Lett.*, 24(23):2198, 2012.

[37] R. Schmogrow, B. Nebendahl, M. Winter, A. Josten, D. Hillerkuss, S. Koenig, J. Meyer, M. Dreschmann, M. Huebner, C. Koos, J. Becker, W. Freude, and J. Leuthold. Error vector magnitude as a performance measure for advanced modulation formats. *IEEE Photon. Technol. Lett.*, 24(1):61–63, 2012.

[38] R. Schmogrow, B. Nebendahl, M. Winter, A. Josten, D. Hillerkuss, S. Koenig, J. Meyer, M. Dreschmann, M. Huebner, C. Koos, J. Becker, W. Freude, and J. Leuthold. Error vector magnitude as a performance measure for advanced modulation formats. *IEEE Photonics Technology Letters*, 24(1):61–63, Jan 2012.

[39] C. E. Shannon. Communication in the presence of noise. *Proceedings of the IEEE*, 72(9):1192–1201, 1984.

[40] J. Skaar and O. H. Waagaard. Design and characterization of finite-length fiber gratings. *IEEE J. Quantum Electron.*, 39(10):1238–1245, 2003.

[41] G. Song and S.-Y. Shin. Design of corrugated waveguide filter by the gel'fand-levitan-marchenko inverse-scattering method. *J. Opt. Soc. Am. A*, 2(11):1985–1915, 1985.

[42] E. G. Turitsina and S. K. Turitsyn. Digital signal processing based on inverse scattering transform. *Opt. Lett.*, 38(20):4186–4188, 2013.

[43] H. V. Aref and Bülow, K. Schuh, and W. Idler. Experimental demonstration of nonlinear frequency division multiplexed transmission. *Optical Communication (ECOC)*, pages 1–3, 2015.

[44] P. J. Winzer and R.-J. Essiambre. Advanced optical modulation formats. *Proceedings of the IEEE*, 94:952–985, 2006.

[45] M. I. Yousefi and F. R. Kschischang. Information transmission using the nonlinear fourier transform, part i: Mathematical tools. *IEEE Trans. Info. Theory*, 60(7):4312–4328, 2014.

[46] M. I. Yousefi and F. R. Kschischang. Information transmission using the nonlinear fourier transform, part ii: Numerical methods. *IEEE Trans. Info. Theory*, 60(7):4329–4345, 2014.

[47] M. I. Yousefi and F. R. Kschischang. Information transmission using the nonlinear fourier transform, part iii: Spectrum modulation. *IEEE Trans. Info. Theory*, 60(7):4346–4369, 2014.

[48] V. E. Zakharov and A. B. Shabat. Exact theory of two-dimensional self-focusing and one-dimensional self-modulation of waves in nonlinear media. *Soviet Phys. JETP*, 34(1):62–69, 1972.

APPENDIX. PRE-COMPENSATION FOR RAMAN SHIFT

The Raman effect brakes the second-order soliton and causes each solitonic component to shift apart inside the symbol time window. Different symbols with different phases encoded on each eigenvalue will breath differently, causing the shift to be different for each symbol. This effect is deterministic and one can equalize and pre-compensate for the pulse shift at the transmitter. Figure A.1 compares the constellation of a regular and a pre-equalized constellation at the receiver.

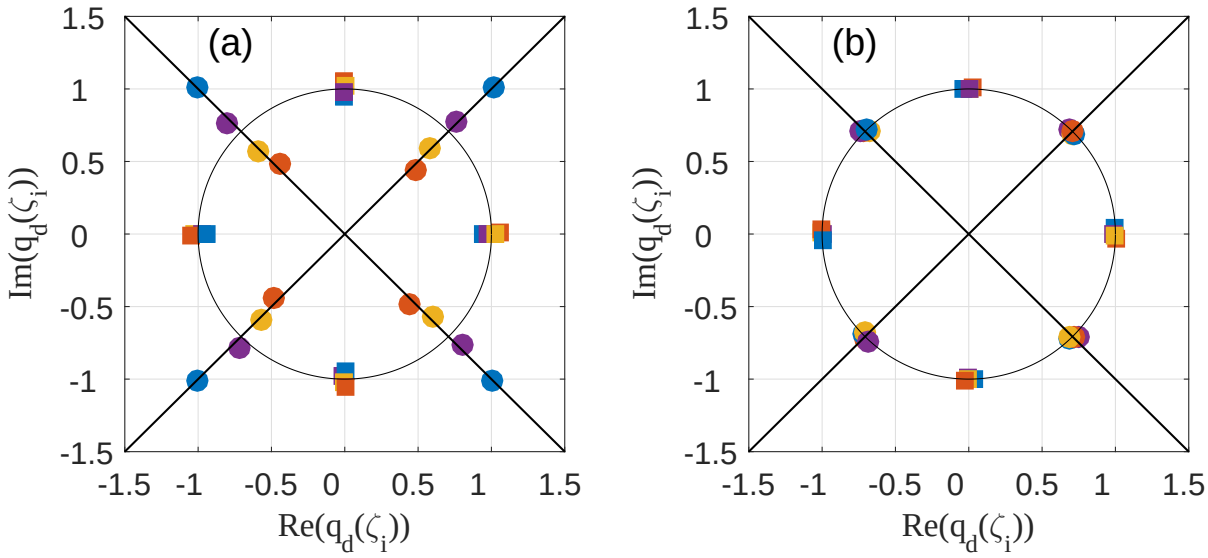

Figure A.1. Constellations recovered at the receiver after 1600 km of propagation distance with the Raman effect and 10.25 dBm launch power. (a) Results of the received constellations without using any equalization technique. (b) Results of the received constellations with the use of a pre-equalized technique.

The equalization technique consists in adjusting the original constellation with enough time and phase shift to address the expected shift in the phase at the receiver due to the Raman effect, which depends on the phase difference between the eigenvalues and.The results of this technique are shown in Figure. A.2.

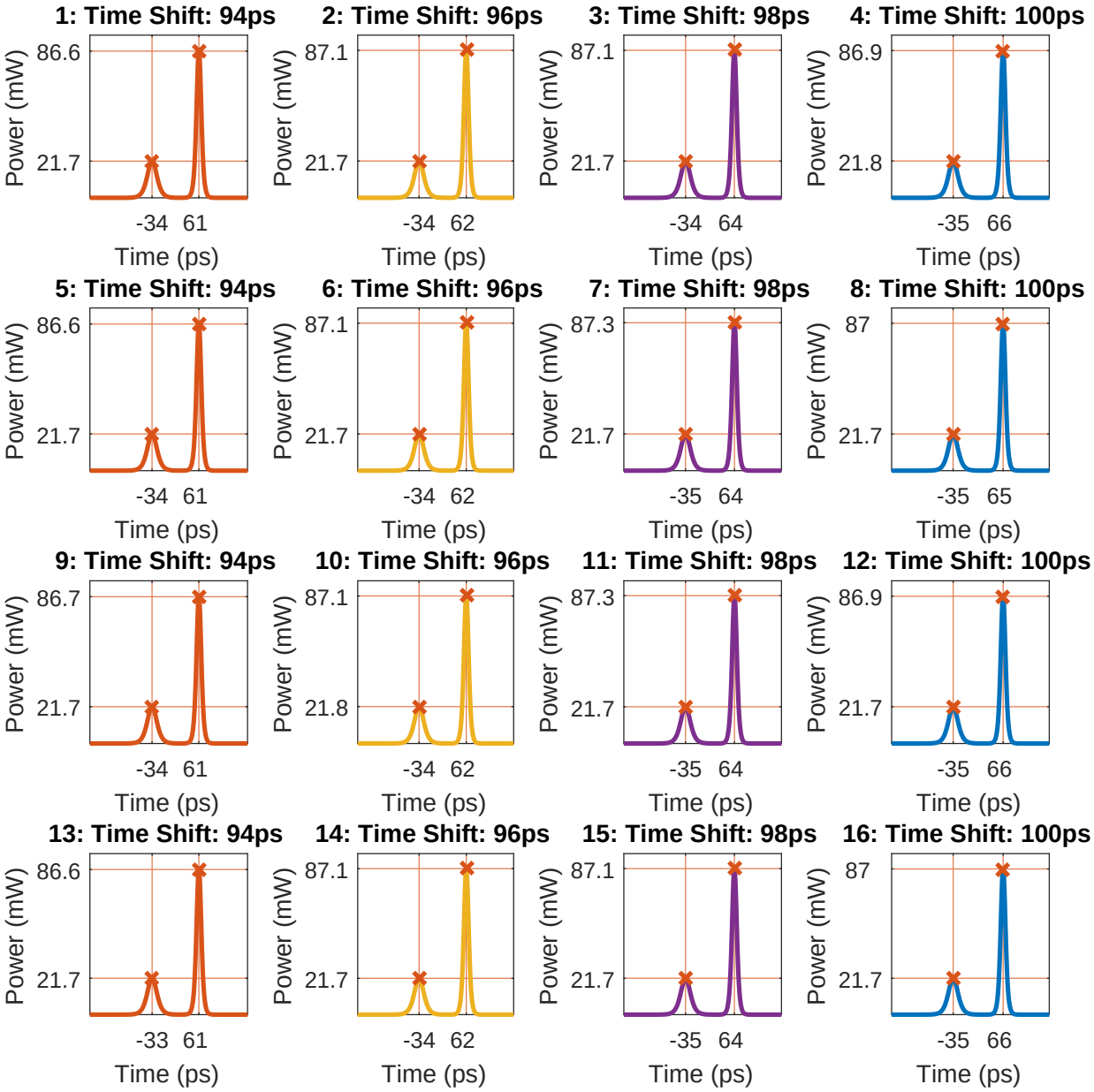

Figure A.2. Waveform of all 16 possible symbols at the receiver when equalization was not used. There are 4 different patterns for each initial phase encoded in the two eigenvalues.